

Toward a Unified Parameterization of the Boundary Layer and Moist Convection. Part III: Simulations of Clear and Cloudy Convection

CARA-LYN LAPPEN AND DAVID A. RANDALL

Department of Atmospheric Sciences, Colorado State University, Fort Collins, Colorado

(Manuscript received 18 July 2000, in final form 31 January 2001)

ABSTRACT

A model that employs a new form of mass-flux closure (described in Part I of this paper) is applied to a variety of clear and cloudy planetary boundary layers (PBLs) including dry convection from the Wangara Experiment, trade wind cumulus from the Barbados Oceanographic and Meteorological Experiment (BOMEX), and marine stratocumulus from the Atlantic Stratocumulus Experiment (ASTEX). For Wangara, the simulated variances and fluxes match that expected from similarity arguments, while the mean state is a little less mixed than the observations. In the BOMEX simulation, the shape and magnitude of the fluxes and the turbulence kinetic energy budget agree with LES results and observations. However, the liquid water mixing ratio is too large. This is attributed to an underprediction of the skewness. In agreement with observations from the ASTEX experiment, many of the model-simulated fields distinctly reflect a regime in transition between the trade wind cumulus and the classic stratocumulus-topped boundary layers.

In general, the simulated entrainment rate tends to be a little underpredicted in regimes where there is little cloud-top radiative cooling (Wangara and BOMEX), while it is overpredicted in regimes where this process is more critical (e.g., ASTEX). Prior work suggests that this may be related to the manner in which the pressure terms are parameterized in the model. Overall, the model is able to capture some key physical features of these PBL regimes, and appears to have the potential to represent both cloud and boundary layer processes. Thus, this approach is a first step toward unifying these processes in large-scale models.

1. Introduction

In Part I of this paper (Lappen and Randall 2001a, hereafter LR1), we described an approach for modeling boundary layer and convective cloud processes within a single framework. In that paper, we derived the equations for a new type of mass-flux closure (MFC) that draws on both higher-order closure (HOC) and previously used MFCs. To accomplish this, we took the familiar “plume” equations describing the mean properties of updrafts and downdrafts and used the mass-flux framework described by Randall et al. (1992) to derive a set of HOC equations. In this framework, all dynamic and thermodynamic quantities are represented with a tophat probability density function (PDF). We call the approach “ADHOC” (Assumed-Distribution Higher-Order Closure). This name directly reflects the approach we used; the tophat PDF is the “assumed distribution,” and the derived higher-order prognostic equations are the “higher-order closure.” The strengths of ADHOC are as follows.

1) It is significantly simpler than a “conventional”

HOC model in that the number of prognostic equations is greatly reduced (in the model, the only prognostic higher-order moments are the fluxes $w'w'$ and $w'w'w'$).

- 2) It provides us with a physically based method to diagnose the updraft area fraction σ and the convective mass flux M_c when $w'w'$ and $w'w'w'$ are known.
- 3) The MFC and HOC equations are completely consistent, term by term; there are no “realizability” issues because all moments are computed from the same PDF.
- 4) A logical way to parameterize the lateral mass exchange terms emerges from their correspondence with the dissipation terms of the HOC equations.
- 5) A subplume-scale (SPS) model accounts for the effects of small-scale motions that cannot be represented with the tophat PDF (Wang and Stevens 1999).

The motivation for constructing such a “unified” cloud/planetary boundary layer (PBL) model was its potential application in general circulation models (GCMs) where arbitrary distinctions are made in transitional regimes (e.g., cumulus-under-stratus, stratocumulus-to-cumulus transition) to separate the “cumulus layer” from the “boundary layer.” Because there is no

Corresponding author address: Dr. Cara-Lyn Lappen, Department of Atmospheric Science, Colorado State University, Fort Collins, CO 80523.

E-mail: lappen@atmos.colostate.edu

clear distinction between these two layers in transitional regions, GCMs do a poor job at simulating the observed cloud fractions (Randall et al. 1998).

In Part II of this paper (Lappen and Randall 2001b, hereafter LR2), we showed results from an ADHOC simulation of trade wind cumulus clouds observed during the Barbados Oceanographic and Meteorological Experiment (BOMEX); in this paper, we show additional results from BOMEX (section 3a), along with results from two additional cases, a dry convective PBL observed during the Wangara experiment (section 2a), and a stratocumulus case from the Atlantic Stratocumulus Experiment (ASTEX; section 4a). For these cases, we compare results to both observations and large eddy simulations (LESs; where available).

The motivation for analyzing three different cases is to explore the limitations of ADHOC under a wide range of conditions. Certain key physical issues are specific to one “type” of regime. If we hope to truly make the ADHOC approach “regime independent” (for incorporation into large-scale models), we need to be aware of its strengths and weaknesses for as many physical situations as possible. Thus, in the conclusions section of this paper (section 5), we assess the strengths and weaknesses of this approach with respect to the wide variety of atmospheric regimes listed above, and we discuss the prospect of incorporating ADHOC into large-scale models.

2. Clear convective PBL

The statistics of free-convective flow are well known from observations (Willis and Deardorff 1974) and LES (Moeng 1984). Turbulence models have had much success simulating dry convection, provided they explicitly account for nonlocal transport [e.g., transilient matrix models (Stull 1988); models with countergradient terms (Holtslag and Moeng 1991); mass-flux models (Wang and Albrecht 1990); and HOC models (André et al. 1978; Yamada and Mellor 1975)].

Below, we show the ADHOC results from the simulation of a clear, convective PBL from the Wangara experiment (Clark et al. 1971). The model needs to represent the following:

- a mean state that is well mixed below the PBL top,
- a linearly decreasing heat flux that becomes negative due to entrainment at the PBL top,
- a vertical velocity variance that is a maximum in the low-to-mid-boundary layer, and
- a horizontal velocity variance that is relatively constant with a near-surface maximum.

The integration is started at 0900 UTC on day 33 (16 August 1967) of the Wangara field study. This day and time were chosen so that we can compare our results directly with those of previous simulations (e.g., André et al. 1978, hereafter A78). This day had clear skies and little horizontal advection of temperature or moisture.

Initial profiles of temperature, water vapor mixing ratio, and winds were taken from Clark et al. (1971) and are depicted in Fig. 1. The surface heat flux is prescribed using Hicks (1978; also depicted in Fig. 1).¹ Following A78, the surface moisture flux is taken to be $1.3 \times 10^{-4} \text{ K}^{-1}$ times the surface temperature flux. Subsidence, horizontal advection, and radiative cooling are assumed to be equal to zero. In the surface layer, wind and temperature variances are estimated according to free convection surface layer similarity [see Eq. (19) in Wyngaard and Coté 1974]. The geostrophic winds are prescribed from observations following Yamada and Mellor (1975). The specifics of the case setup are shown in Table 1.

Results and discussion

In this section, we show the Wangara results for the mean state, turbulent fluxes, and momentum variances. We will compare these to the results of A78 and to observations. Figure 2 shows the observed mean potential temperature (θ) and water vapor mixing ratio (\bar{q}_v), along with those simulated by ADHOC and A78. ADHOC does a reasonable job at simulating a well-mixed θ profile, although it does not appear to be as well mixed as either A78 or the observations in the lower part of the boundary layer (the unstable surface layer is deeper in ADHOC than in the observations). However, the differences between ADHOC and the observations at hour 12, for example, are small compared with the differences between the hour-12 profiles and the initial profiles. In other words, the ADHOC boundary layer evolves in a realistic manner. The stable nighttime surface layer is mixed out in a reasonable amount of time, and the period of rapid PBL growth (which occurs as the mixed layer rises through the nighttime neutral layer) occurs near hour 11, in agreement with the observations. At the PBL top, there is an “overshoot” region where thermals penetrate into the inversion. Because the overshoot region in the ADHOC simulations is not as large as that of A78 or that observed, the ADHOC thermals do not penetrate as far into the inversion (this can also be seen in Fig. 3). However, the ADHOC-simulated boundary layer grows to ~ 1400 m by hour 16 (1600 UTC) in agreement with the observations and A78. This is discussed below.

Because radiative cooling and advection are negligible for this day, a well-mixed quasi-steady θ profile implies a linear heat flux ($w'\theta'$) profile. This is depicted in Fig. 3, which shows that the profiles are linear over the depth for which θ is well mixed. The magnitude of the negative flux at the PBL top is an indicator of the

¹ One should note here that the surface heat flux used by A78 was derived from the Clark et al. (1971) data, while that used by ADHOC was prescribed from the observations of Hicks (1978). The forcing is in general very similar; however, there are some small differences around hours 12–14 (see Fig. 3).

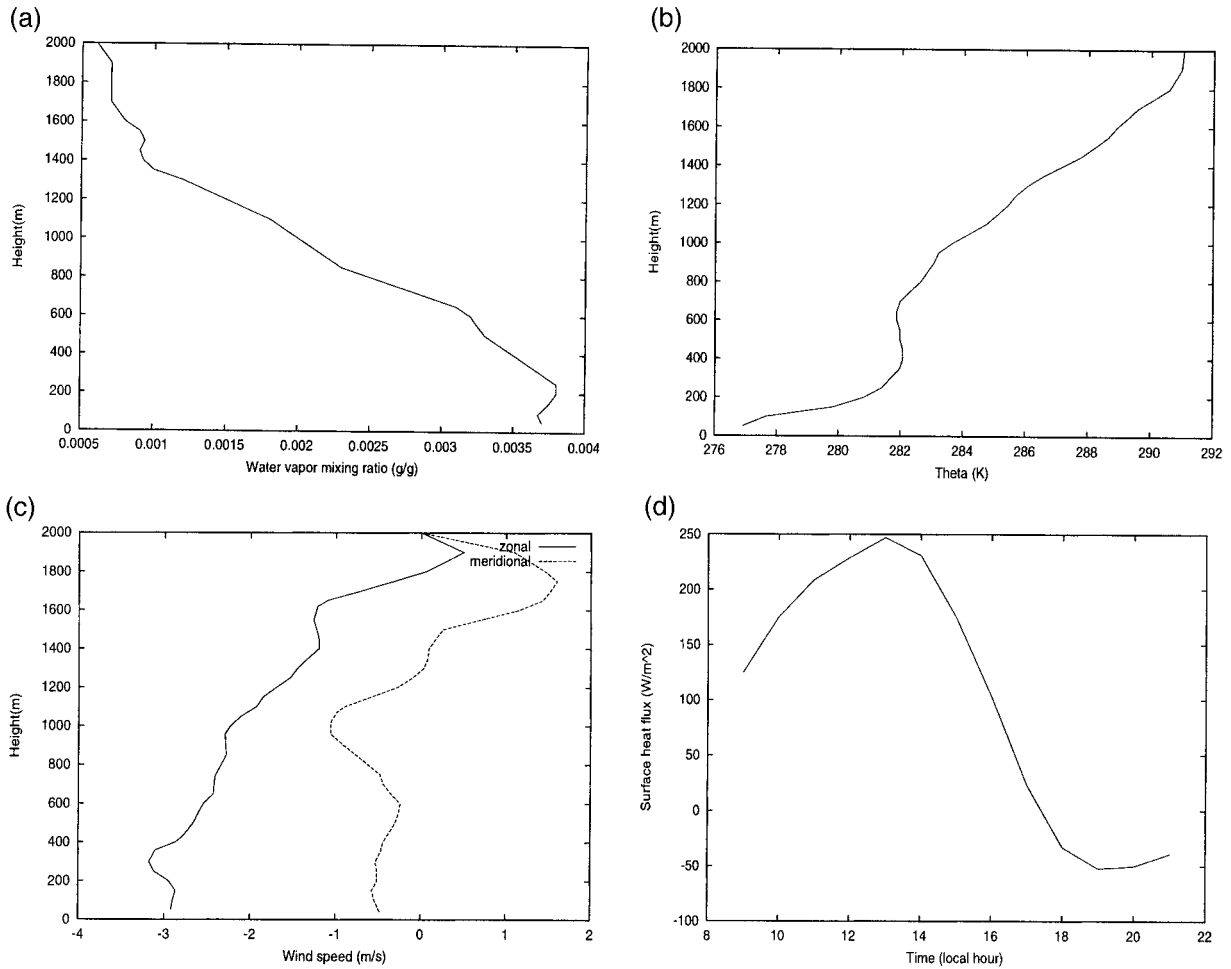


FIG. 1. Initial mean-state profiles for Wangara: (a) water vapor mixing ratio, (b) potential temperature, and (c) zonal and meridional winds. (d) Imposed surface heat flux.

TABLE 1. Model setup and forcing for Wangara, BOMEX, and ASTEX runs.

	Wangara	BOMEX	ASTEX
Surface sensible heat flux (SHF)	Hicks (1978); see Fig. 1	Constant in time at $8 \times 10^{-3} \text{ K m s}^{-1}$	Constant in time at $1 \times 10^{-2} \text{ K m s}^{-1}$
Surface latent heat flux	$1.3 \times 10^{-4} \times \text{SHF}$	Constant in time at $5.2 \times 10^{-5} \text{ m s}^{-1}$	Constant in time at $1 \times 10^{-5} \text{ K m s}^{-1}$
Radiative cooling	None	Prescribed function of height	Prescribed function of the liquid water path
Horizontal moisture advection	None	Prescribed function of height	None
Horizontal temperature advection	None	None	None
Subsidence	None	Prescribed function of height	None
P_{sfc} (mb)	1023	1015	1029
T_{sfc} (K)	Changes in time	300.375	292.5
Time step (s)	0.5	0.5	0.5
Grid spacing (m)	50	40	25
Length of simulation (h)	12	16	4
Number of levels	40	75	60
Time period plotted	Instantaneous	Average over hours 12–16	Average over hours 2–3

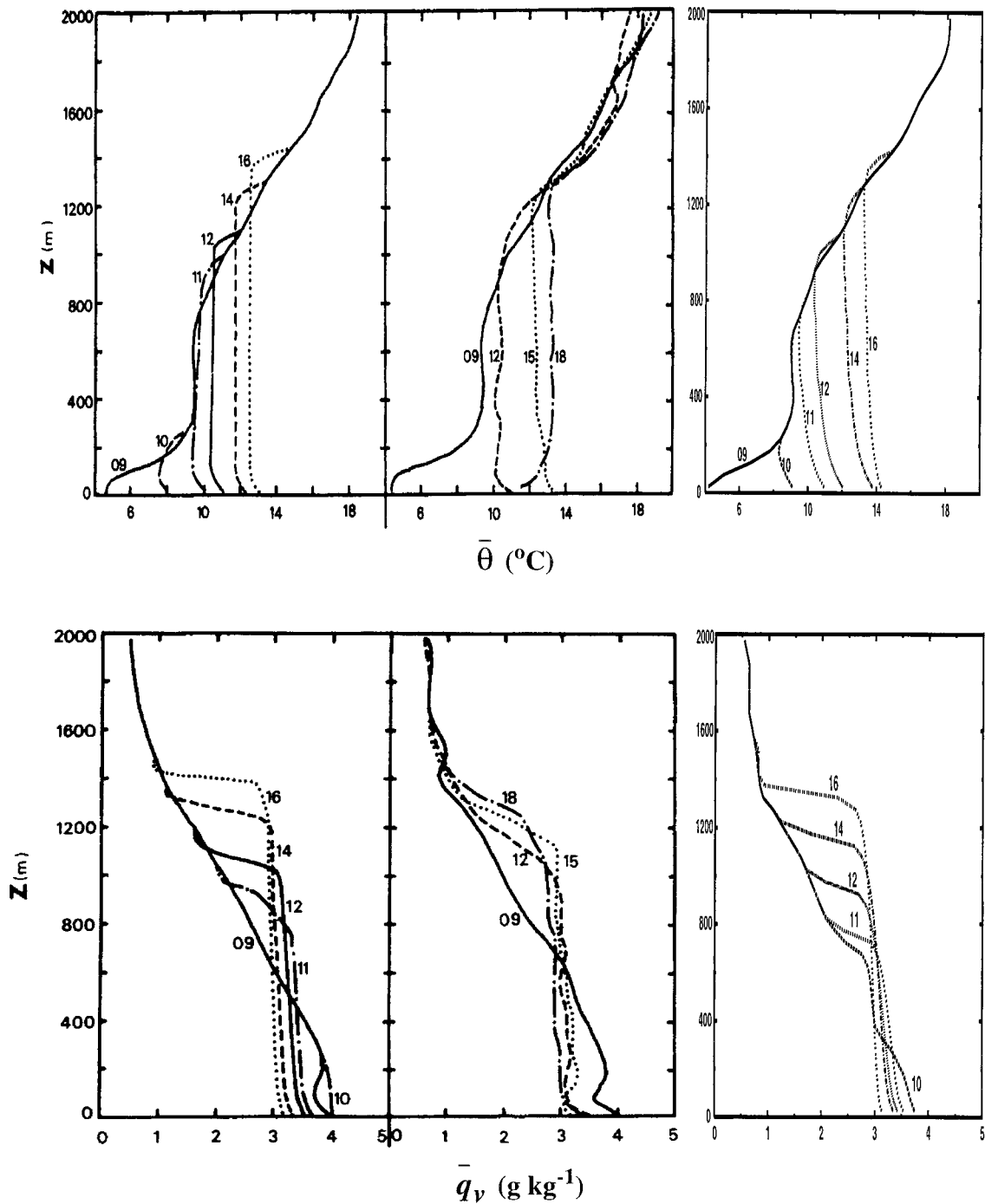


FIG. 2. Comparison of the (right column) ADHOC-simulated (top row) potential temperature and (bottom row) water mixing ratio with those simulated by (left column) A78 and (middle column) that observed for Wangara. The left and middle column plots are taken from A78.

entrainment rate. By hour 14 (1400 UTC), this flux is a maximum likely indicating that the PBL is entraining most rapidly. By hour 16, the surface has begun to cool radiatively, and the weaker thermals that result do not penetrate as far as during midday. At hour 14, the magnitude of the maximum negative heat flux is -0.14 times

the surface flux.² This is less than that found by applying similarity relationships to the free-convective PBL (-0.2 ; Stull 1988), but it is close to that obtained by

² This value was -0.10 and -0.15 when the grid resolution was halved and doubled, respectively.

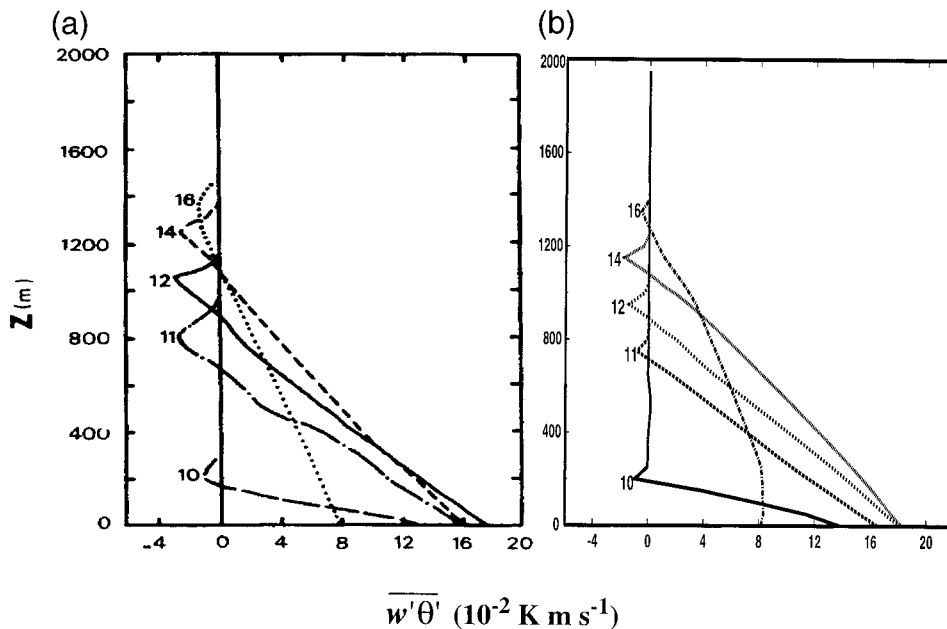


FIG. 3. Comparison of the (b) ADHOC-simulated potential temperature flux with that simulated by (a) A78 for Wangara.

A78 (-0.15). Since the depth of the PBL by hour 16 is close to that observed, however, ADHOC must produce encroachment to arrive there. While we expect encroachment during the period when the top of the newly forming mixed layer passes through the height of the residual neutral layer, we expect PBL growth to be mostly a result of entrainment after the mixed layer reaches the inversion. This is not the case in ADHOC. Between hours 12 and 14, a comparison of the area between the $\bar{\theta}$ profiles in Fig. 2 and the area under the surface heat flux curve in Fig. 1 shows that 75% of the mixed-layer growth through the inversion is due to encroachment [see Stull (1988, p. 455) for a description of this technique].

In Fig. 4, we compare the ADHOC-simulated moisture flux with that of A78. Unlike the heat flux profile, the moisture flux profile is not perfectly linear. This occurs because the \bar{q}_v distribution is not quasi-steady in time, especially near the PBL top (see Fig. 2). The slope of the moisture flux profile is positive in the bulk of the PBL because the boundary layer becomes drier over time (Fig. 2). The shapes of the simulated flux profiles agree well with known relationships in dry convective PBLs (e.g., Stull 1988).

The dimensionless profiles of the turbulence kinetic energy (TKE) are shown in Fig. 5. The variances of horizontal ($u'u' + v'v'$) and vertical ($w'w'$) momentum are nondimensionalized with the free-convective velocity scale,

$$w^* = (g\alpha z_i Q_0)^{1/3}, \quad (1)$$

where g is the gravitational acceleration, α is the coefficient of thermal expansion for air, z_i is the mixed

layer depth, and Q_0 is the surface heat flux. These dimensionless profiles are stationary as the PBL evolves, in agreement with mixed-layer similarity. The vertical velocity variance exhibits a characteristic profile, with a maximum at $z/z_i = 0.3$ in agreement with that found by applying similarity theory to the dry convective PBL [Stull 1988; note that the location of the maximum near this level is somewhat expected due to our choice of lateral mixing constants (see LR2)]. The horizontal momentum variance is largest near the ground, where downdrafts spread out horizontally. It is well mixed in the bulk of the PBL and drops to zero at the PBL top.

For completeness, we show the temperature variance normalized by the convective temperature scale ($T^* = Q_0/w^*$) in Fig. 6 and the momentum fluxes in Fig. 7. While the momentum fluxes are a little weaker than those of A78 near the PBL top, the agreement is generally good. As discussed in LR1, the applicability of a top-hat model for momentum fluxes is questionable. In ADHOC, the momentum fluxes are predicted using traditional HOC [Bougeault 1982; for a more complete description of momentum fluxes in ADHOC, see LR1 and Lappen (1999)].

The temperature variance shows maxima at the inversion and near the surface. The inversion maximum is a result of penetrating thermals entraining warmer air into the PBL top. Here, we see that the temperature variance simulated by ADHOC is less than that of A78. As discussed, the thermals generated by ADHOC do not entrain as efficiently as those observed or as those simulated by A78. Since ADHOC is relying on encroachment for PBL growth, we would expect a temperature variance that is too small at the inversion. In addition,

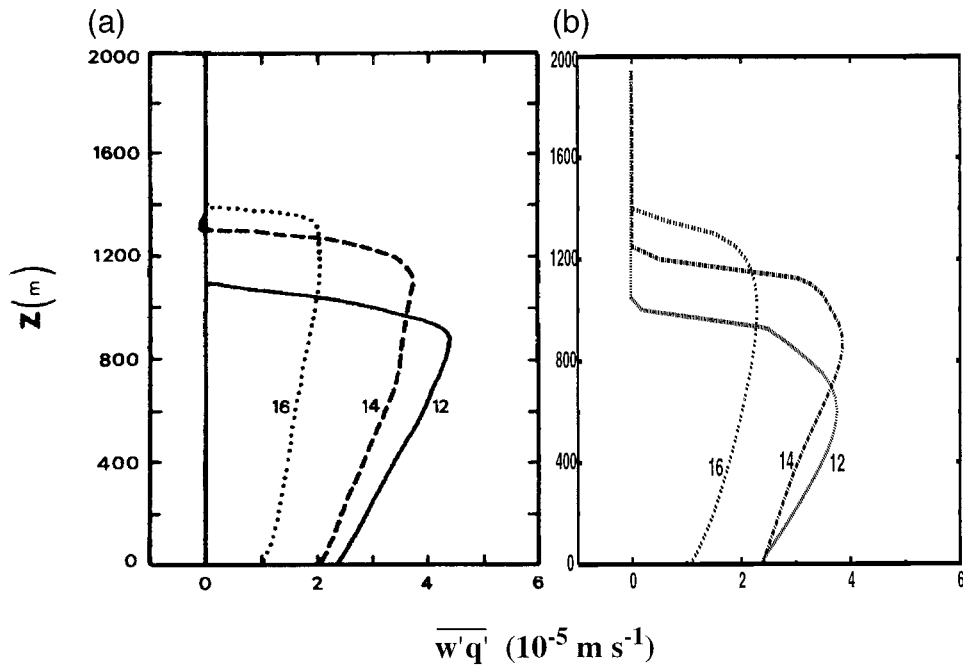


FIG. 4. Comparison of the (b) ADHOC-simulated water mixing ratio flux with that simulated by (a) A78 for Wangara.

thermodynamic variances in ADHOC are not predicted—they are diagnosed with tophat formulas (see LR1). Young (1988, using observations) and Wang and Stevens (2000, using LES results) show that thermodynamic variances are underrepresented with tophat formulas.

In general, ADHOC does a reasonable job of simulating day 33 of Wangara. However, the θ profile has a deeper unstable region near the surface than is observed, indicating that nonlocal heat transport in ADHOC may not be strong enough. Also, as discussed above, PBL-top entrainment is too weak. Tests show that the weak

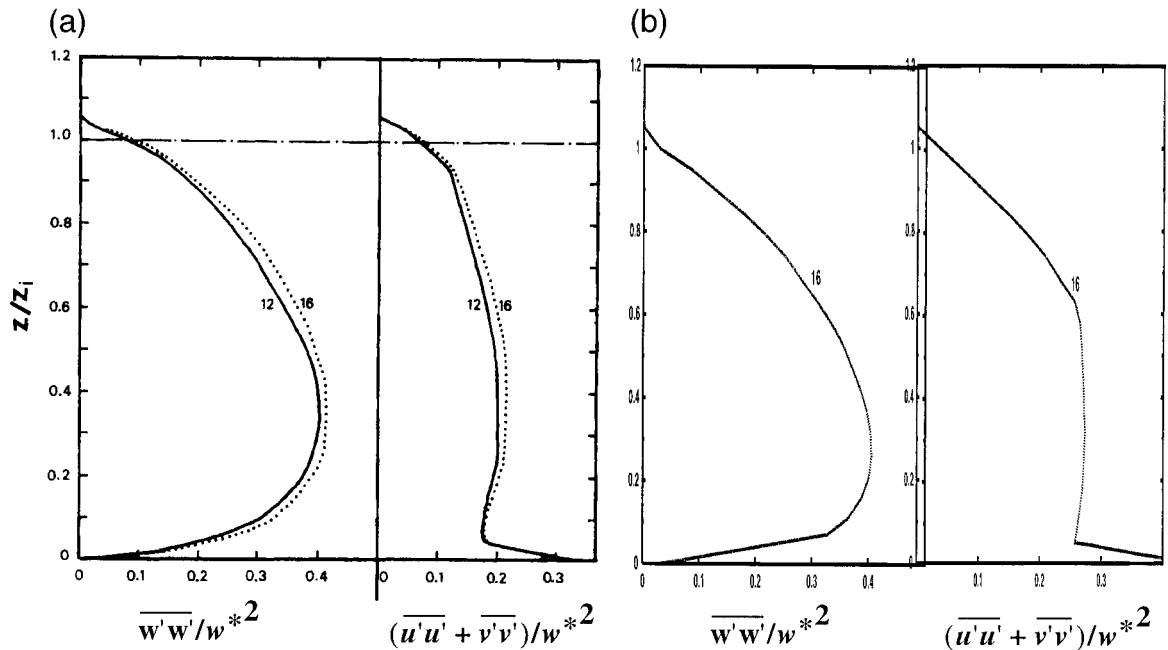


FIG. 5. Comparison of the (b) ADHOC-simulated momentum variances with those simulated by (a) A78 for Wangara. The variances are normalized by the free-convective velocity scale.

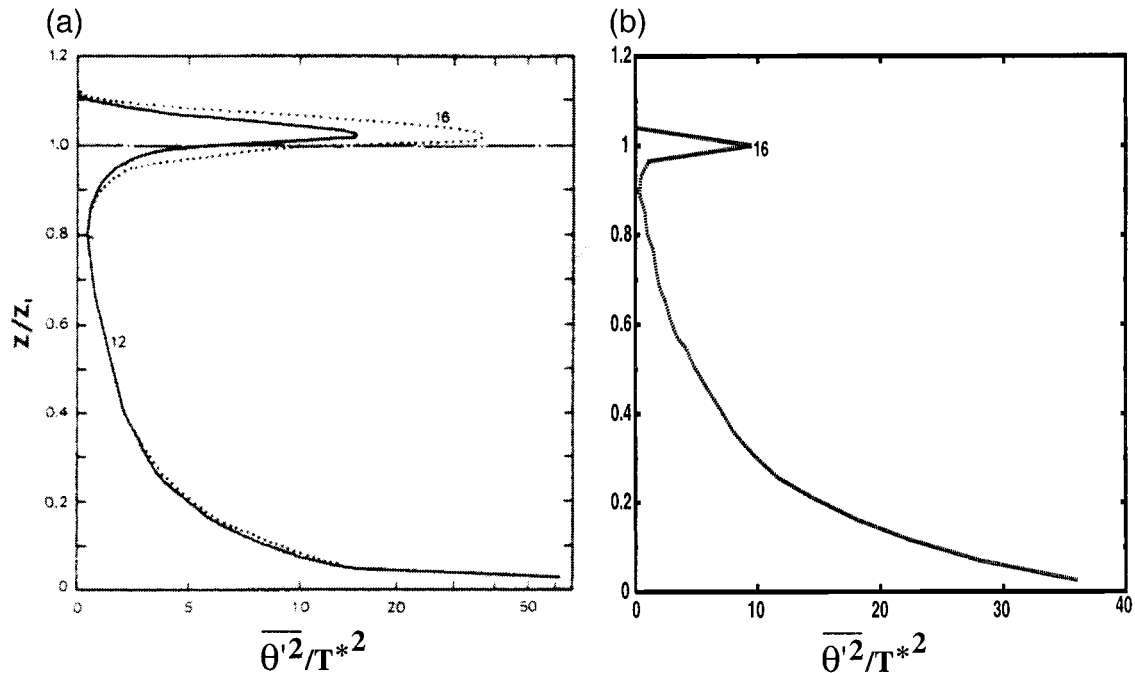


FIG. 6. Comparison of the (b) ADHOC-simulated temperature variance with that simulated by (a) A78 for Wangara. The variance is normalized with the free-convective temperature scale.

entrainment may be related to how the pressure terms are modeled in ADHOC (we use the same form as that used in HOC models; Rotta 1951; Launder 1975; LR1). As air ascends toward the inversion, a pressure gradient acts to slow it down. As it slows, the air spreads out horizontally. The efficiency with which the pressure slows the air influences the entrainment rate. If the parameterized pressure term is too efficient, then all of the vertical motion gets converted into horizontal motion, and very little is left to penetrate the inversion and drive the entrainment process. If the pressure term is inefficient, most of the energy remains in the vertical to drive entrainment. We have shown (Lappen 1999, Fig. 17) that small adjustments to the pressure term can significantly enhance the entrainment rate. Further study is needed here.

Despite weak PBL-top entrainment and mean-state profiles a little less mixed than observed, ADHOC does a reasonable job simulating the turbulence statistics of free convection. Since free convection is dominated by large eddies, mass-flux models such as ADHOC are naturally suited for such a regime. In the next two sections we look at some more complicated regimes, namely, trade wind cumulus and the marine stratocumulus that were observed during ASTEX. While large eddies³ certainly play a role in these regimes, small eddies are also important.

³ Large describes eddies whose depth is comparable to cloud depth (for shallow cumulus) and to the PBL depth (for dry convection and stratocumulus).

3. Trade wind cumulus

The presence of trade wind cumuli significantly intensifies the plume-scale atmospheric dynamics. The convective mixing of heat and moisture associated with these clouds increases the surface evaporation. This moisture is transported downstream by the Hadley circulation and eventually fuels deep cumulus (Cu) convection in the intertropical convergence zone (ITCZ; Nitta 1975; Yanai et al. 1976). Deep Cu clouds are responsible for the upward energy transport needed to balance the export of potential energy in the outflow regions of the convection. This whole process is “fueled” by trade wind Cu. Thus, in order to accurately represent large-scale dynamics in GCMs, we must first be able to accurately parameterize the effects of trade wind Cu.

Locally, the effects of the trade wind Cu are also important. In the subtropics, the environmental sounding is conditionally unstable, but only through a shallow layer. This promotes the development of shallow (often nonprecipitating) clouds. Although Cu in this regime are shallow, they are crucial for maintaining the trade wind inversion against the large-scale subsidence in the descending branch of the subtropical Hadley circulation. Deeper Cu activity, which is found near the ITCZ, is suppressed by subsidence in the trade wind regime.

Despite the importance of the trade wind Cu regime for the large-scale dynamics, only a few parameterizations used in large-scale models treat shallow convection explicitly [e.g., Tiedtke (1989), which is cur-

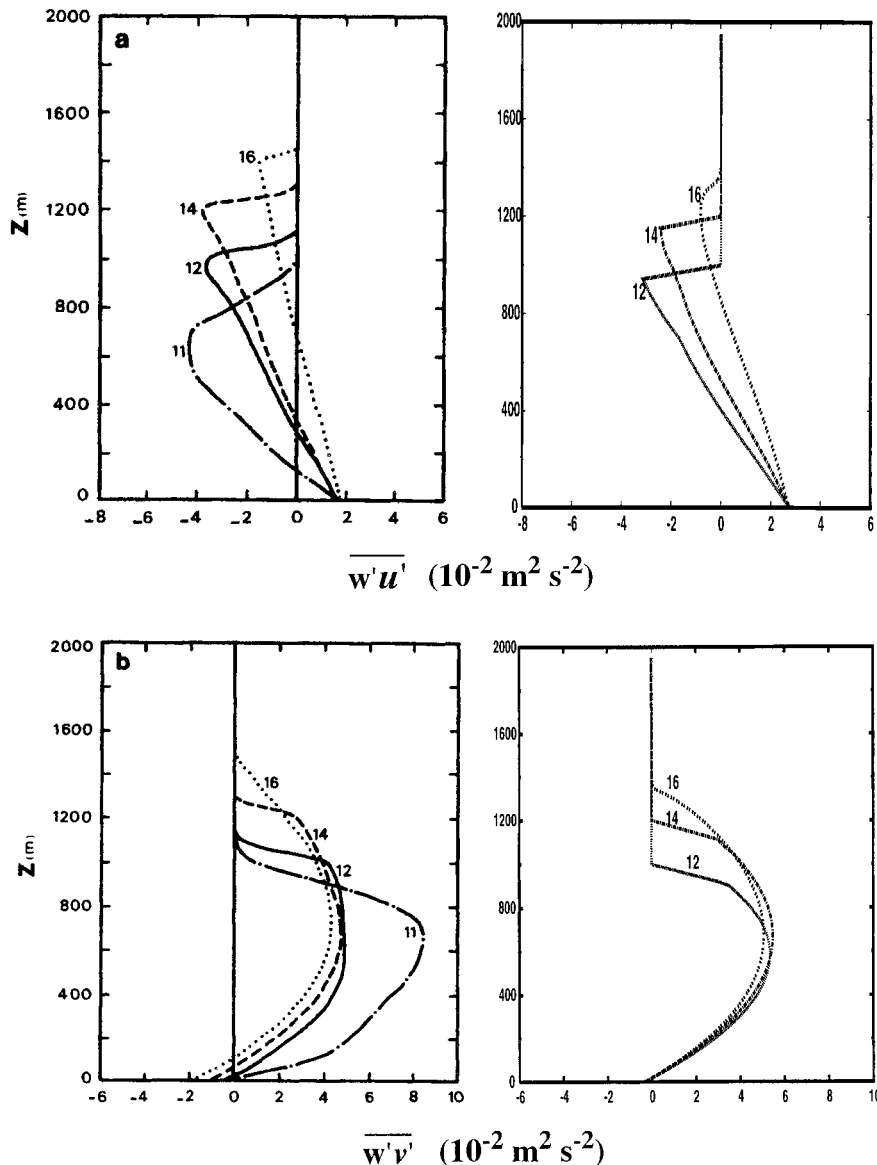


FIG. 7. Comparison of the (right column) ADHOC-simulated momentum fluxes with those simulated by (left column) A78 for Wangara (top row, zonal flux; bottom row, meridional flux).

rently used in the European Centre for Medium-Range Weather Forecasts parameterizations, and Gregory and Rowntree (1990), which is operational in the Met Office parameterizations. The importance of including the trade wind regime in convection schemes has been demonstrated by Tiedtke (1988), but in most GCMs, shallow convection is ignored. We should note there that the cumulus parameterization of Arakawa and Schubert (1974) is technically able to represent these clouds, but in practice it does not produce enough shallow clouds to fully represent this regime. The coarse resolution in large-scale models is one reason.

Observations show that trade wind cumulus clouds have a four-layered structure: a well-mixed subcloud

layer, a conditionally unstable cloud layer, a thin slightly stable layer between the two, and an inversion layer (see Fig. 8). Unlike stratocumulus (Sc) clouds, Cu exist in a dry, stably stratified *environment* that is nonturbulent.

Currently, there exist four types of models to represent the trade wind boundary layer (TWBL) (Bechtold et al. 1995): 3D LES models (Somméria 1976; Cuijpers and Duynkerke 1993), which resolve cumulus circulations explicitly but have small domains; 2D cloud ensemble models (Krueger 1988; Krueger and Bergeron 1994), which cover a mesoscale domain; 1D HOC models, which make use of a subgrid scale condensation scheme (Bougeault 1981a,b); and mixed layer or “bulk” models (Betts 1973; Albrecht 1979) in which the bound-

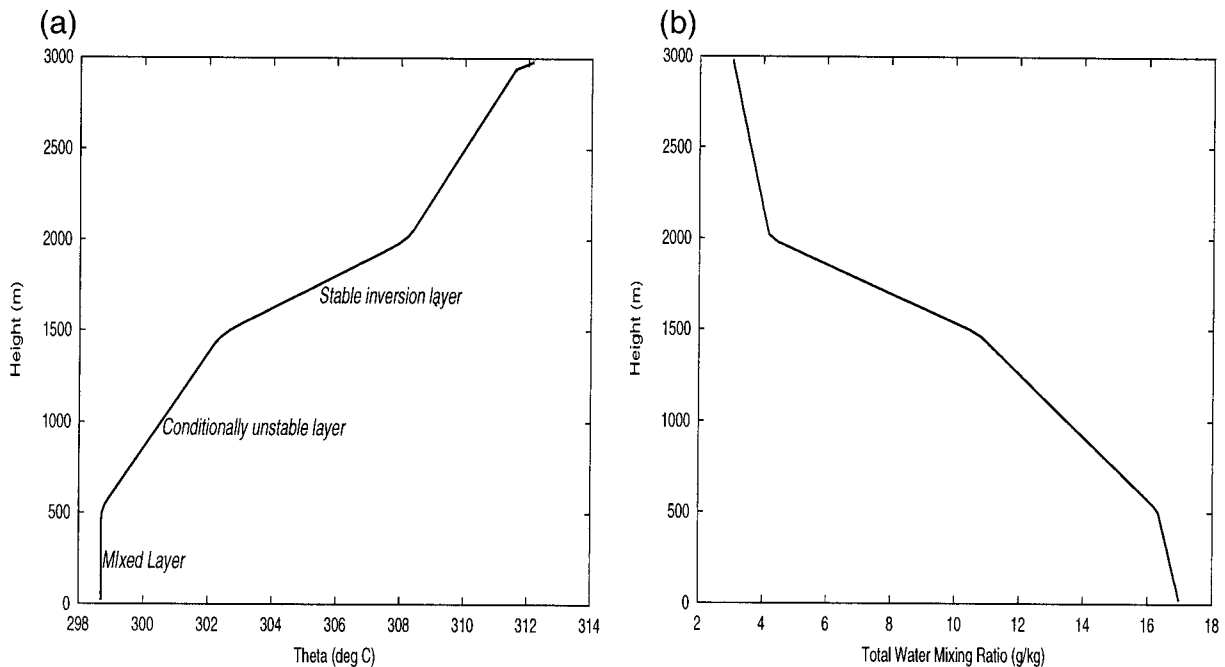


FIG. 8. Initial profiles of the (a) liquid water potential temperature and (b) total water mixing ratio for BOMEX. The three-layered structures of the trade wind cumulus regime are so marked.

ary layer is typically represented by one layer of variable depth and the turbulent fluxes in the PBL are computed from only the surface flux and the entrainment rate.

LES is the most successful method for modeling this regime because it explicitly resolves the convective circulations (Somméria 1976; Pennell and LeMone 1974; Siebesma and Cuijpers 1995).

One-dimensional HOC models, which parameterize both the convective circulations and the small-scale turbulence, typically have difficulties modeling Cu clouds (Yamada and Mellor 1979). This is because conventional closures typically assume that turbulence is nearly isotropic and nearly Gaussian (Lumley 1978), whereas Cu regimes are highly nonisotropic and non-Gaussian (Bougeault 1982). Modified HOC models have fared better. For example, Bougeault (1981a) developed a special turbulence condensation scheme with the help of the LES results of Sommería (1976) for a 1D HOC simulation of the TWBL. Bechtold et al. (1995) developed a scheme in which he linearly interpolated between Gaussian turbulence profiles and a distribution with known constant positive skewness. In this scheme, he tuned the skewness to a “trade-wind-specific” value.

One-dimensional mass-flux models applied to the TWBL are tuned to be trade wind specific (e.g., Albrecht 1979). In general, mass-flux schemes have been used only in conjunction with mixed-layer models for simulating the trade wind Cu layer (Hanson 1981; Betts 1976; Albrecht 1979). As a result, there are some questions that mass-flux models have been unable to answer. How does the cumulus ensemble affect the mixed layer

turbulence? How can we parameterize the lateral mixing between the cumulus updrafts and the environment?

Krueger and Bergeron (1994) noted that 2D cloud ensemble models currently contain the minimum level of complexity to simulate the TWBL without special tuning. Two such models have had success in modeling this regime: Sun and Ogura (1980, a second-order closure scheme) and Krueger and Bergeron (1994, a third-order closure scheme).

ADHOC differs from earlier mass-flux models in that it represents the higher-moment turbulence statistics of the boundary layer, whereas previous mass-flux models represented only the mean-state quantities. In this section, we show results from the ADHOC simulation of the trade wind Cu case BOMEX.

BOMEX

BOMEX took place 22–30 June 1969 near Barbados. We ran this case using the setup outlined by the Global Energy and Water Cycle Experiment (GEWEX) Cloud System Studies (GCSS; Browning 1994) boundary layer working group I. (A complete summary of the case is available online at <http://www.knmi.nl/~siebesma/bomex.html>.) An abbreviated description is given in Table 1, and the initial profiles of potential temperature and mixing ratio are shown in Fig. 8. A brief description of the BOMEX field study can be found in LR2.

The results here are meant to supplement those shown in LR2. There we showed that, in order to accurately simulate the in-cloud turbulence and subcloud layer

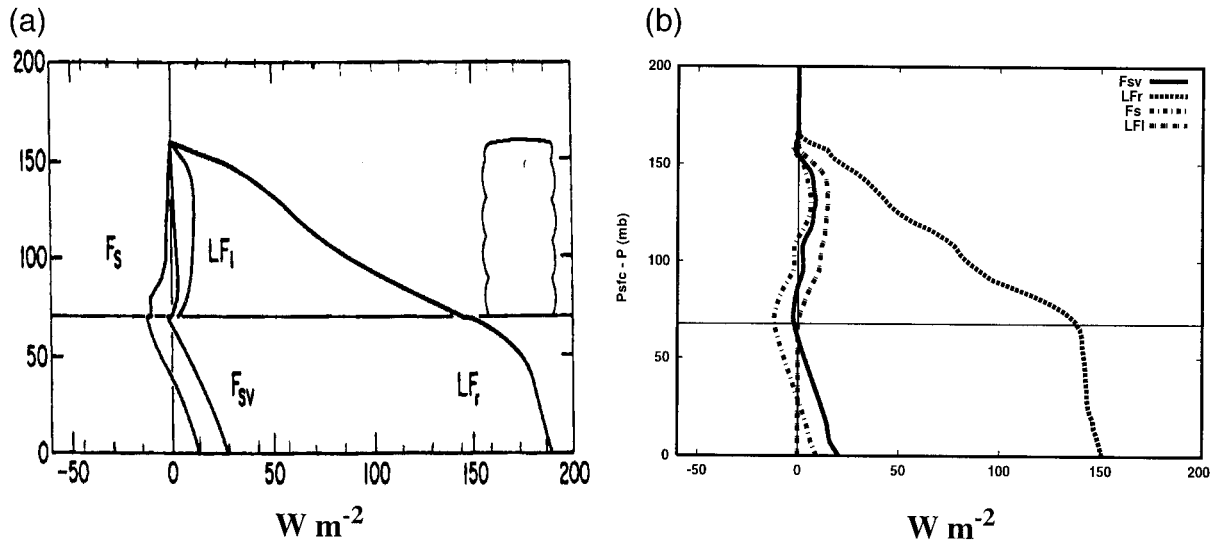


FIG. 9. Comparison of the (b) BOMEX-simulated and (a) observed fluxes of dry static energy (F_s), virtual dry static energy (F_{sv}), total water (LF_r), and liquid water (LF_t). The observed profiles are from Esbensen (1978).

mixing in BOMEX, the SPS fluxes must be represented. In LR2, we compared the mean state, turbulent fluxes, and variances from ADHOC and LES simulations of BOMEX. Here we will compare the ADHOC fluxes to observations and the TKE budget to that simulated by LES.

Figure 9 depicts the observed and simulated fluxes of water vapor, liquid water, and virtual dry and dry static energies. ADHOC successfully represents the shapes of these profiles, as well as their relative magnitudes. The sensible heat flux is downward, with a maximum at cloud base. The profiles of the virtual and dry static energies are parallel below the cloud but merge together as cloud top is approached. In ADHOC, the two are practically the same in the upper part of the cloud layer. This means that the increase in buoyancy due to large amounts of water vapor is offset by the decrease due to liquid water. The simulated liquid water flux reaches its maximum value just below cloud top. The maximum at cloud top is much less pronounced in the observations however. In LR2, we showed that the simulated liquid water mixing ratio is too high, and in section 2a, we showed that for the Wangara case, the entrainment rate is too weak at the PBL top. These two factors combine to produce a liquid water flux maximum near cloud top (entrainment in BOMEX acts dry out the region near cloud top). For BOMEX, we also found (as we did in Wangara) that there is a weak dependence of the entrainment rate on grid resolution (not shown).

It is interesting that the buoyancy flux also shows a maximum near cloud top despite the large value of the liquid water loading there. The maximum in the sensible heat flux that occurs at this height outweighs the liquid water loading effect on the virtual static energy flux. The maximum in the sensible heat flux is a result of the

strong condensational heating associated with the excess of liquid water.

We note here that the BOMEX GCSS case is highly idealized; the prescribed forcing is constant and cannot adjust to the evolving dynamic and thermodynamic fields (see Table 1). The “real atmosphere” obviously adjusts. Thus, while the shape of the ADHOC flux profiles matches that observed, we do not expect the magnitudes to be exact (e.g., the total water flux).

Figure 10 shows the TKE budgets simulated by ADHOC and LES. The buoyancy production rate profile is that of a classic trade wind cumulus layer. It is positive near the surface (from surface sensible and latent heat fluxes) and in the cloud (from latent heat release), and slightly negative in between. The ADHOC-simulated buoyancy flux profile has the right shape and magnitude but drops to zero at a lower altitude than the corresponding LES flux profiles. It appears that the convection top simulated by ADHOC is too low. We also saw this in LR2 in the vertical velocity variance ($\overline{w'w'}$) plot. However, the heat and moisture fluxes depicted in LR2 show that the PBL depth in ADHOC matches that simulated by LES. There is a difference in the depth of the LES boundary layer if one compares plots of the LES fluxes and $\overline{w'w'}$ (this difference does not exist in ADHOC). Since this difference occurs in $\overline{w'w'}$ only, it is probably caused by the presence of gravity waves in the LES, which are not represented in ADHOC. It is curious that the buoyancy flux profile matches that of LES, while ADHOC’s liquid water mixing ratio is too large (see Fig. 6 in LR2). We will discuss this below.

The other TKE budget terms are also well simulated by ADHOC. The shear term has the correct shape; the turbulent transport shows the export of TKE from the surface to the subcloud layer and from cloud base to

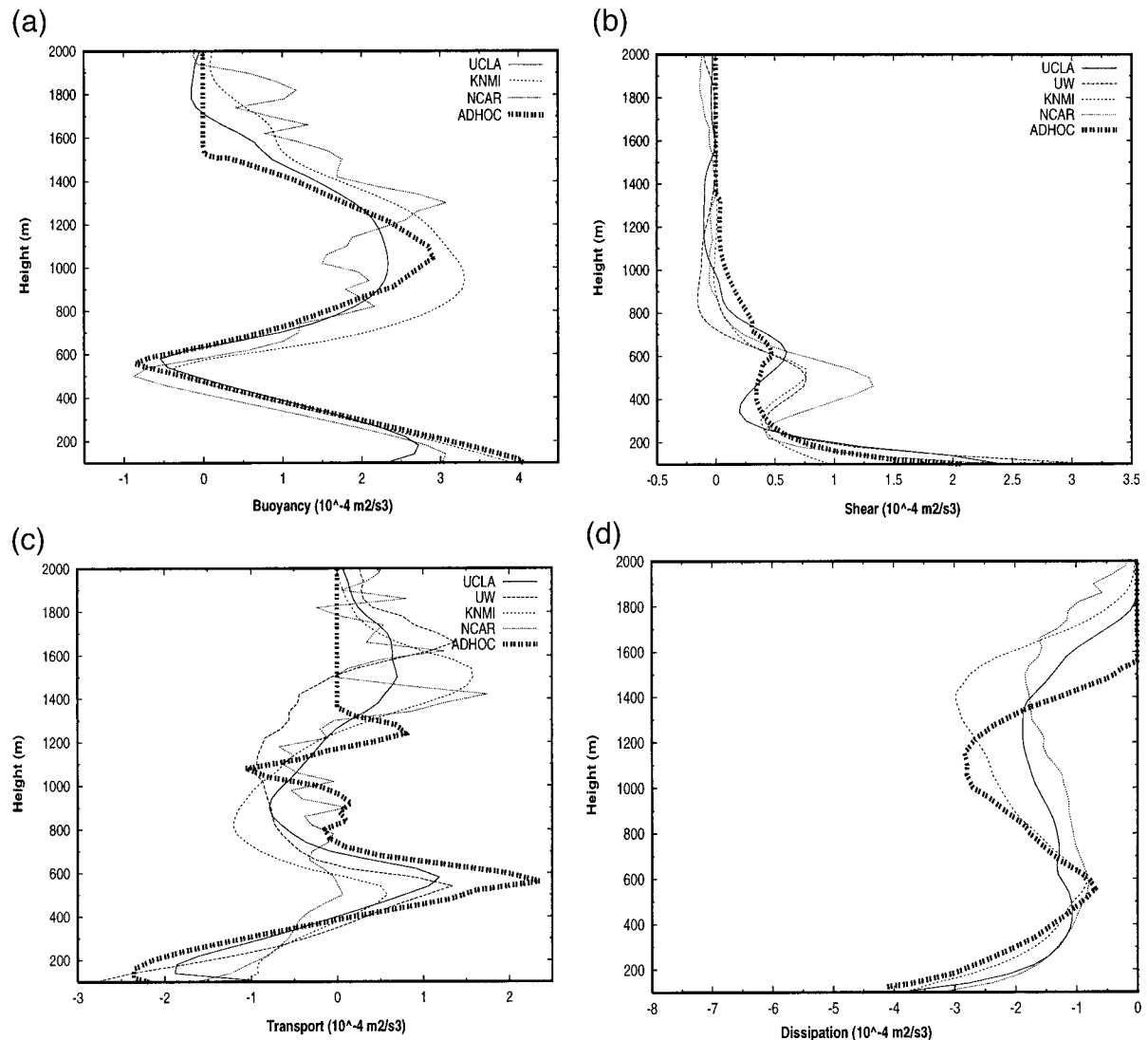


FIG. 10. Comparison between ADHOC and LES simulations of the TKE budget for BOMEX. (a) Buoyancy, (b) shear, (c) turbulent transport, (d) dissipation. The darkest line is ADHOC, while all other lines are the indicated LES models.

cloud top (TKE is transported out of regions where it is produced); and the dissipation rate is largest where the TKE is largest. We see that ADHOC is able to simulate a physically correct picture of the mechanisms, which generates turbulence for the BOMEX case.

The final plots that we will show are ones that highlight the mass-flux aspect of ADHOC. Figure 11 shows the simulated vertical velocity skewness and the updraft and downdraft liquid water mixing ratios. The former is compared with LES results. The shape of the ADHOC-simulated skewness agrees with that simulated by LES; however, the magnitude is too small (by a factor of 3 in the cloud). This may explain the apparent discrepancy (discussed above) between the ADHOC-simulated buoyancy flux (Fig. 10) and liquid water mixing ratio (Fig. 6 in LR2). ADHOC appears to get the correct buoyancy flux, despite overproducing cloud liquid wa-

ter, by underrepresenting the skewness. Smaller positive skewness means the updraft area is too large [see Eq. (10) in LR1]. Since liquid water is concentrated in the updrafts (for BOMEX), a larger than observed updraft area is consistent with an overprediction of liquid water.

The ADHOC-simulated shape of the skewness profile makes physical sense, however, when one considers the structure of the trade wind cumulus regime. As discussed above, thermals are generated near the surface and at cloud base. Thus, one would expect higher updraft area fractions in these regions. The skewness shows a relative minimum in both these places in accord with higher σ values [see Eq. (10) in LR1]. As thermals leave these regions, fewer and fewer have the energy to penetrate higher. Thus, the number of thermals is expected to decrease as the subcloud and cloud layer tops are approached. Thus, we would expect larger pos-

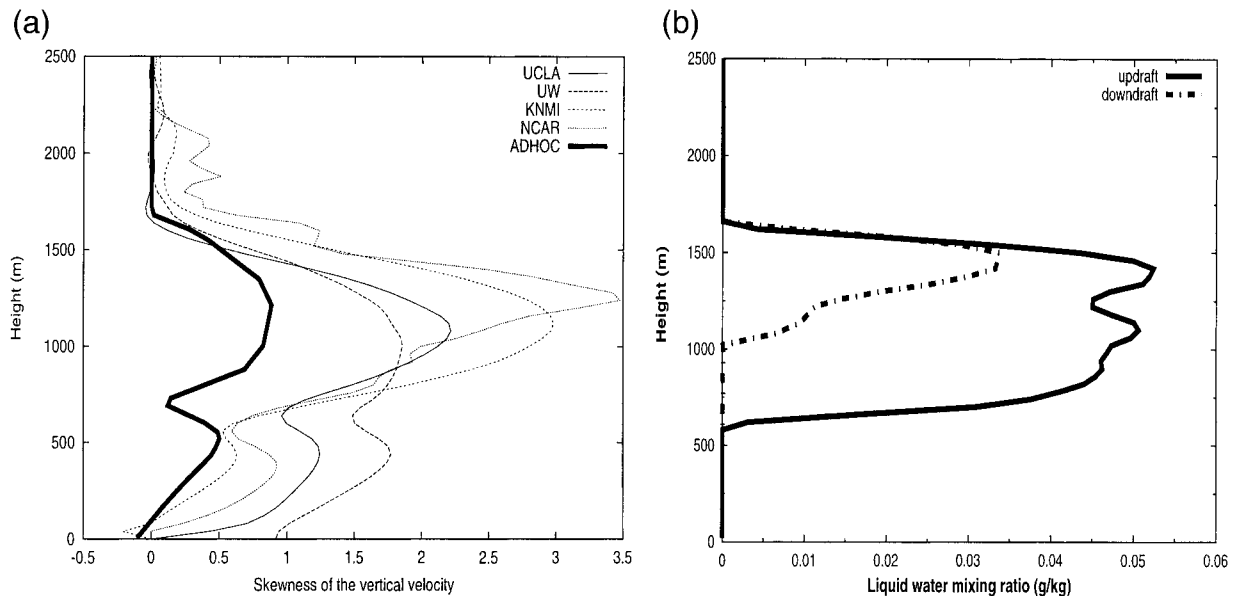


FIG. 11. (a) Updraft area fraction and (b) the updraft and downdraft liquid water mixing ratios simulated by ADHOC.

itive skewness (lower σ) under cloud base and near cloud top. Finally, the skewness decreases at cloud top (σ increases) due to the thermals spreading out as they impinge upon the inversion.

The updraft and downdraft liquid water mixing ratios are also depicted in Fig. 11. In BOMEX, we would expect to have partly cloudy layers in which the downdrafts are completely dry. We see that this is true in the lower layers of the cloud. In the upper layers, the downdraft is significantly drier than the updraft, but it is not liquid-free. We saw in LR2 that the *mean* liquid water mixing ratio simulated by ADHOC was too large. We also saw in section 2 that the entrainment rate in ADHOC is too weak. The combined effect of these two factors is such that the air does not completely dry out as it enters the top of the downdraft. Thus, ADHOC simulates an anvil-like region at cloud top (this was not observed). As the air descends in the downdraft, this small amount of liquid water quickly evaporates to form a partly cloudy layer.

4. Marine stratocumulus

Marine stratocumulus (MSc) clouds are globally important from both radiative and dynamical standpoints. These low-level marine clouds are significant modulators of the earth's radiation budget (Hartmann et al. 1992). They increase the overall albedo but have little effect on the longwave radiation emitted to space. Satellites show that the net cloud forcing by MSc can locally be as large as -100 W m^{-2} , and globally is approximately -17 W m^{-2} during the Northern Hemisphere summer (Ramanathan 1989; Harrison et al. 1990). In addition, Slingo (1990) showed that modest changes in low-cloud amount, liquid water content, or

droplet size in MSc could cause climatically significant changes in the global radiation budget.

From a dynamical standpoint, MSc can significantly modify the tropical general circulation (Tiedtke 1988). They are found in the subtropics, upstream of trade wind Cu. The MSc-topped boundary layer (ScTBL) differs from the TWBL in that the inversion strength is stronger and the sea surface temperatures are cooler. While both the ScTBL and the TWBL modify the large-scale circulation by maintaining the trade wind inversion, the physical mechanisms are different in these two regimes. In the MSc regime, all cloud layer motions occur under saturated conditions, while in the trades, the subsiding motions are unsaturated. In addition, a ScTBL is turbulent throughout the entire layer while the Cu regime is only turbulent in the cloud; the region between the clouds is rather quiescent.

The turbulent/convective dynamics of Sc are driven primarily by radiative cooling of air parcels near cloud top (Lilly 1968; Duynkerke et al. 1995; Nicholls 1984, 1989). This cooling drives turbulence, which in turn drives the entrainment of warmer, drier air into the cloud top, thereby causing droplets to evaporate. This can lead to even more cooling and more turbulence. It has been proposed that this process, called cloud-top entrainment instability (CTEI; Lilly 1968; Randall 1980; Deardorff 1980; Siems et al. 1990), can eventually lead to the breakup of the cloud deck. Clearly, the crux of accurately simulating MSc is the proper representation of the entrainment process. Other processes that play a role in the ScTBL include surface latent and sensible heat fluxes, drizzle, and solar absorption in the cloud layer. The latter two of these can lead to "decoupling" of the subcloud and cloud layers (Brost et al. 1982; Nicholls 1984; Betts 1990; Wang and Wang 1994).

Most numerical investigations of the ScTBL have evolved from Lilly's (1968) mixed-layer approach. For this application, mixed-layer models (also called bulk models) have had much success (Randall and Suarez 1984; Turton and Nicholls 1987; Bechtold et al. 1996). The major shortcoming of bulk models is their inability to predict the evolution of the PBL in situations where 1) local transport dominates (e.g., shear-driven boundary layers) or 2) the PBL is not well mixed. To overcome these deficiencies, many cloud modelers explored second-order closure to model the ScTBL.

In a cloudy PBL regime, thermodynamic variances and covariances are important to determine the cloud amount and fractional cover (Somméria and Deardorff 1977). This means that second-order closure modelers must employ a level-four⁴ Mellor–Yamada scheme (or higher) if they wish to diagnose such features. Early studies that applied such schemes to the ScTBL included Oliver et al. (1978) and Moeng and Arakawa (1980). In general, however, these level-four Mellor–Yamada models tended to underpredict entrainment fluxes. They attributed this to the use of a downgradient assumption for the third-order moments. Due to the importance of entrainment fluxes in the ScTBL, many cloud modelers abandoned second-order schemes and turned to third-order closure (Chen and Cotton 1983; Moeng and Randall 1984; Krueger 1988).

Bougeault and André (1986) made a major breakthrough toward the goal of accurately modeling the ScTBL. They formulated a new dissipation length scale that depends on a harmonic average of the upward and downward “free paths” of a parcel. Interestingly enough, Bechtold (1992) was able to simulate the ScTBL with a *second*-order closure model when they adopted this scheme, along with the subgrid-scale condensation scheme of Sommeria and Deardorff (1977).

Mass-flux models have also had success in modeling the ScTBL. Observations show that fluxes in the ScTBL can be represented using mass-flux formulas [Eq. (3) in LR1; Penc and Albrecht 1987; de Laet and Duynkerke 1998]. Despite these observations, however, very few cloud modelers have used the mass-flux approach to model the ScTBL. The few studies that have used this method employ mixed layer models, along with the mass-flux parameterization (e.g., Wang and Albrecht 1986). We performed simulations with ADHOC of MSc clouds that were observed during ASTEX using the setup outlined by the GCSS boundary layer working group I (information available online at <http://www.fys.ruu.nl/~wwwimau/ASTEX/astexcomp.html>).

ASTEX

ASTEX took place 1–28 June 1992 over the northeastern Atlantic Ocean (Albrecht et al. 1995). One of

its principal goals was to characterize the evolution of cloudiness and vertical structure in a marine boundary layer as it moves over a warmer surface (Bretherton and Pincus 1995). The aim of the field project was to understand the transition from Sc to Cu in the subtropics.

The 1996 ASTEX GCSS case (number 209N) was designed using the data from the first ASTEX Lagrangian (L1) study, which took place from 12 to 14 June 1992. It is a 3-h simulation that begins at 0400 UTC 13 June 1992. During this time, the Azores high was well established and the winds were NNE at 10 m s^{-1} . Throughout the time period Sc with sustained drizzle was observed. In this simulation, we used the no-drizzle setup (available online at <http://www.fys.ruu.nl/~wwwimau/ASTEX/astexcomp.html>). During L1, extensive aircraft measurements were taken (de Rooze and Duynkerke 1997). One of these aircraft, the NCAR Electra, flew during the times represented in this simulation (flight RF06). In the next section, we will compare the ADHOC results for this case to these aircraft measurements, as well as to LES results.

The initial conditions, the large-scale forcing, and the model specifics for this case are shown in Table 1. The prescribed initial conditions and subsidence forcing are very different from those of the BOMEX case. In general, the ScTBL is characterized by colder SSTs and weaker latent heat fluxes. Due to weaker surface fluxes, the cloud-top inversion in ASTEX occurs at a lower height (650 m) than in BOMEX (1000 m). The strength of the inversion (defined as the “jump” in potential temperature divided by the height over which the jump occurs) is only slightly larger for ASTEX than for BOMEX. This is reflective of the fact that ASTEX is not a classic ScTBL (e.g., Sc which forms off the coast of California), but is more representative of a transitional regime in between the TWBL and the classic ScTBL (discussed below). Large-scale models have difficulty representing this regime (LR1).

From a turbulence standpoint, the classic ScTBL has more in common with Wangara than with BOMEX (e.g., the mean states are both well mixed, the flux profiles are linear, the vertical velocity variances are parabolic with a maximum in the middle of the boundary layer). However, because ASTEX is a transitional regime between the TWBL and the ScTBL, we often see characteristics of both these regimes in ASTEX. We will thus compare the turbulence statistics of ASTEX to those of both the classic ScTBL and BOMEX.

In the top panels of Fig. 12, we show a comparison among the mean-state vapor and liquid water mixing ratios simulated by ADHOC and LES, and observed with aircraft. In general, ADHOC agrees with the aircraft observations quite nicely. Although ADHOC simulates less liquid water than that simulated by LES, ADHOC agrees better with the observations. (The maximum liquid water mixing ratio observed was approximately 0.42 g kg^{-1} .) This is also shown in Table 2, where the integrated liquid water path in ADHOC is

⁴ A level-four Mellor–Yamada scheme refers to a HOC model in which all second moments are predicted (Mellor and Yamada 1974).

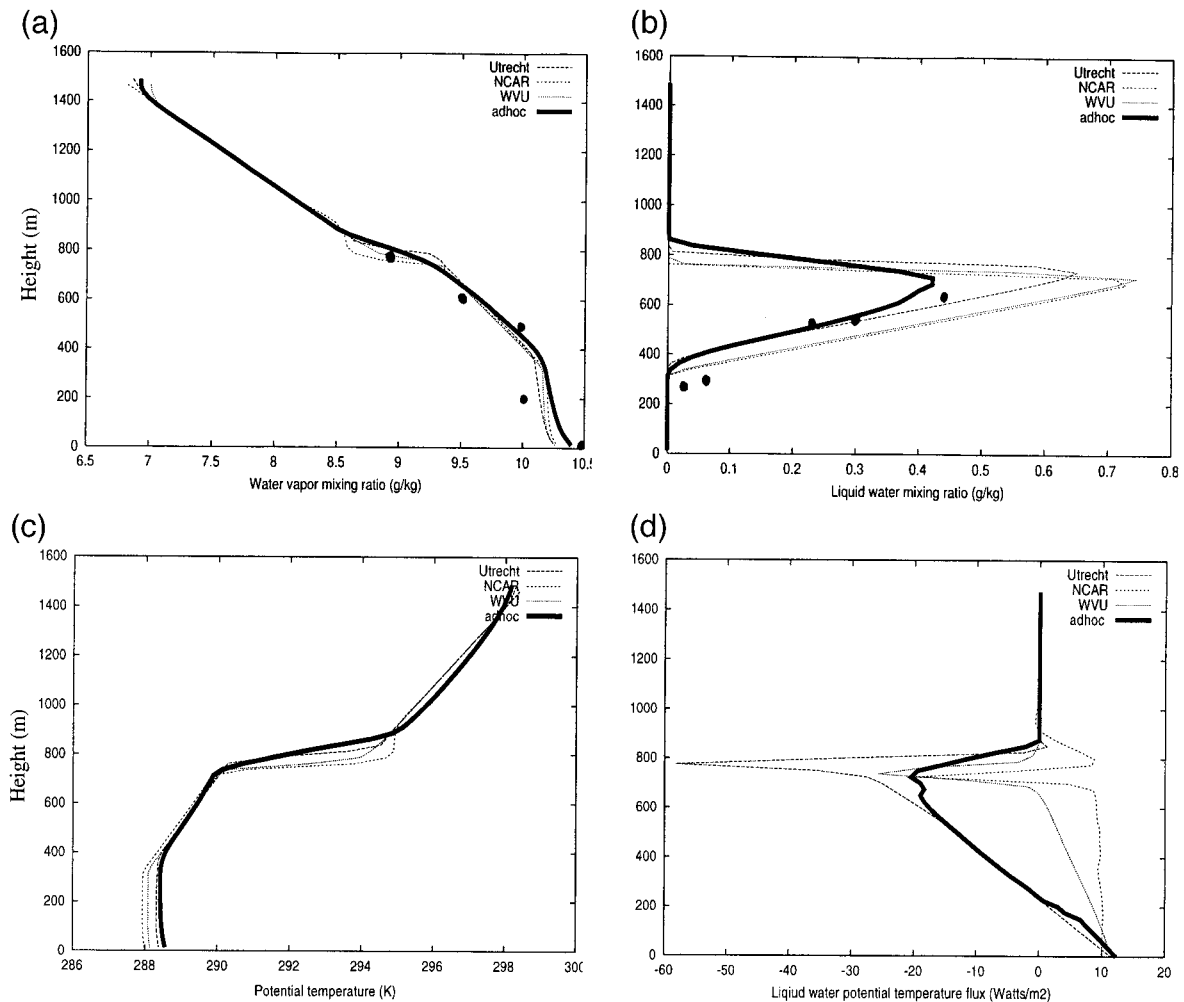


FIG. 12. Comparison of the (a) simulated mean water vapor and (b) liquid water mixing ratios, (c) liquid water potential temperature, and (d) liquid water potential temperature flux for ASTEX with that of LES and observations. The darkest line is ADHOC, the lighter lines are the indicated LES models, and the dots are observations from the NCAR Electra as analyzed by de Roode and Duynkerke (1997).

TABLE 2. Comparison of entrainment and scaling parameters for ADHOC, LES, and observations. An "x" indicates that the data was unavailable.

	ADHOC	Observations	Utrecht LES	NCAR LES	Met Office LES
Zi (m)	767	x	797	747	759
Integrated					
LWP (g m^{-2})	151	x	176	182	177
We (m s^{-1})	0.014*	x	0.011	0.010	0.012
w^* (m s^{-1})	0.5	0.66	0.7	0.9	0.8
u^* (m s^{-1})	0.29	0.28	x	x	x
T^* (K)	0.008	0.01	x	x	x
q^* (g kg^{-1})	0.022	0.027	x	x	x

* This value is 0.009 and 0.016 when the grid resolution is halved and doubled, respectively.

less than that simulated by LES. Since the liquid water in a ScTBL is mainly determined by processes that occur at cloud top, this discrepancy likely reflects a difference between the amount of entrainment drying simulated by ADHOC and LES. Table 2 shows that ADHOC is in fact entraining faster than the LES models. Interestingly enough, the weak entrainment found with Wangara and BOMEX is not a problem in ASTEX. The reasons for this are discussed below.

In the bottom panels of Fig. 12, we show a comparison between the mean-state liquid water potential temperature (θ_L) and liquid water potential temperature flux ($w'\theta_L'$) simulated by ADHOC and LES. In general, the boundary layer is a little warmer than that simulated by LES near the surface. The flux, $w'\theta_L'$, has some scatter, even among the LES results. The θ_L profile shows the transitional nature of the ASTEX regime. It is not as well mixed as that in a typical Sc cloud, but the temperature difference between cloud base and cloud top

is not as large as that in the TWBL. Thus, the magnitude of the slope is a cross between a well-mixed (vertical) profile and the slopes seen in the trade wind regime BOMEX (see Fig. 8).

At the top of the cloud layer in ASTEX, we would expect a “jump” in $w'\theta'_L$ due to the strong radiative cooling occurring there. We see this jump in the LES results, but not in ADHOC. This is an indication that 1) radiative cooling is not as strong in the ADHOC simulations as it is in the LES, 2) entrainment warming is overly efficient in the ADHOC simulation and it partially cancels the effect of radiative cooling, or 3) a combination of both of these is occurring. The simulated radiative flux profiles (not shown) show that the radiative cooling rate in ADHOC is less than that of the LES (the liquid water path is smaller; see Fig. 52 of Lappen 1999). In addition, Table 2 shows that the entrainment rate in ADHOC is comparable to that simulated by LES (although it has a weak dependence on grid resolution; see footnote in Table 2). Thus, not only is the radiative cooling smaller, the modulation due to entrainment warming is larger (larger in a relative sense; i.e., for a given amount of radiative cooling, there is more entrainment warming).

In this simulation, it appears as if radiative cooling is *overly* efficient at driving entrainment [although less cooling is occurring at cloud top, the entrainment rate and the average height of the PBL top are comparable between the LES and ADHOC (Table 2)]. This is the opposite of the conclusion found for BOMEX. In ASTEX, the inversion strength is slightly stronger than in BOMEX, while they both have a similar radiative cooling rate. What factors control the differences in the way these two regimes process the radiative cooling that results in ASTEX being able to entrain inversion air while BOMEX is less efficient at this process?

From a physical standpoint, other processes can occur at cloud top besides radiative cooling and entrainment warming. A big difference between ASTEX and BOMEX, with regard to cloud top, is the updraft–downdraft liquid water differences. In BOMEX, the downdraft is significantly drier than the updraft (depending on the location in the cloud; Fig. 11). In ASTEX, the updraft and downdraft liquid water mixing ratios are virtually the same. Dry downdrafts warm adiabatically. Moist downdrafts warm more slowly due to the evaporation of liquid water. Thus, the additional cooling due to the evaporation of liquid water in the downdrafts permits enough additional turbulence that entrainment can be maintained.

While this may explain why ADHOC gives larger entrainment for ASTEX than for BOMEX, more explanation is needed as to why ADHOC overpredicts the entrainment rate *relative to LES* for ASTEX and underpredicts it (relative to LES) for BOMEX. A possible explanation may be that a large fraction of the radiative cooling in ASTEX is occurring within the stable temperature gradient in the mean inversion. This is referred

to as “direct cooling” in Lewellen and Lewellen (1998). In that paper, this effect was responsible for the enhanced entrainment seen by some models with coarser grid resolution in a radiatively cooled smoke cloud intercomparison. We note in Table 2 (in the footnote) that ADHOC’s entrainment rate can vary with vertical resolution for ASTEX.

The same strong LES radiative cooling that produced the cloud-top “spike” of $w'\theta'_L$ (Fig. 12), also is responsible for the LES-simulated spike in the liquid water flux $w'r'_L$ (Fig. 13). Note that this spike does not occur in the total water flux $w'r'_T$. This is a result of offsetting spikes (similar in magnitude but opposite in sign) between $w'r'_L$ and the water vapor flux $w'r'_v$ (the latter flux profile is not shown). Aside from this spike, ADHOC is able to accurately simulate the magnitude and shape of the liquid and total water fluxes.

Before moving on to a discussion of the variances and the TKE budget, we would like to do a brief comparison of the ADHOC flux results with observations. Figure 14 shows $w'r'_T$ and the virtual static energy flux $w's'_v$, simulated by ADHOC and observed with aircraft. Overall, the shape and magnitude of the observed $w's'_v$ profile is well represented by ADHOC, while the simulated $w'r'_T$ profile is too strong. It is not too surprising that the simulated *in-cloud* flux of $w'r'_T$ is larger in ADHOC than it should be; entrainment not only warms but also dries. The larger drying that occurs in the ADHOC simulation is directly responsible for a larger upward moisture flux; one that is needed to replenish the loss and maintain a steady state. However, the LES fluxes depicted in Fig. 13 are also larger than those observed. The inclusion of drizzle in these simulations reduces the total water flux to that observed (information available online at <http://www.fys.ruu.nl/~wwwimau/ASTEX/astexcomp.html>). The effects of drizzle are not included in ADHOC.

The profile of $w's'_v$ simulated by ADHOC is more typical of a TWBL, where the surface and the cloud layer are almost decoupled (the virtual static energy flux is slightly negative between the two). This is almost identical to the shape simulated in the BOMEX case (see Fig. 7 in LR2). However, the magnitude of the negative flux is much smaller percentagewise (compared with the magnitude of the surface flux) in ASTEX than in BOMEX. This reflects the transition away from the TWBL regime, toward the more classic ScTBL. The observations clearly support the ADHOC-simulated profile.

Next, we examine the simulated vertical velocity variance and TKE budget and compare them to those of LES and observations (Figs. 15–16). The simulated vertical velocity variance ($w'w'$) is significantly different than that of two of the LES models, with the largest difference being in the center of the PBL. However, $w'w'$ simulated by ADHOC agrees quite nicely with the observations and with the Utrecht LES (the latter only in the upper boundary layer).

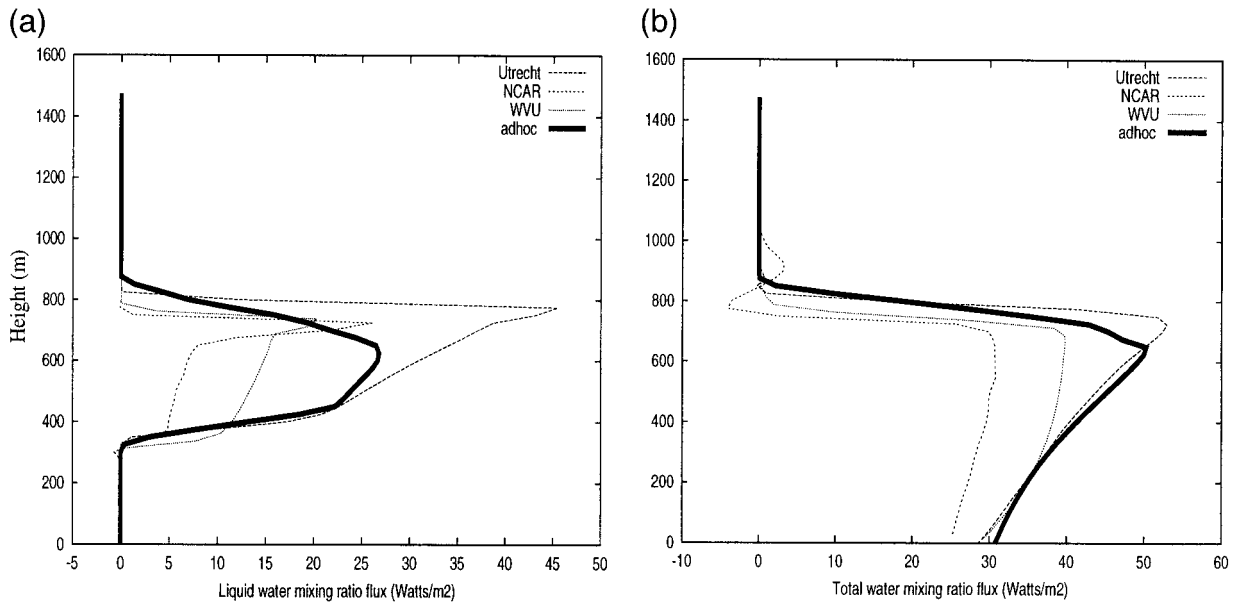


FIG. 13. Comparison of the ADHOC- and LES-simulated fluxes for ASTEX of (a) liquid water and (b) total water. The darkest line is ADHOC and the lighter lines are the indicated LES models.

Here again, ADHOC shows that the ASTEX regime has some TWBL characteristics, but that they are more transitional in nature than BOMEX. The profile of $w'w'$ in BOMEX has two distinct maxima (one in the cloud and one in the subcloud layer), with a significant minimum in between (see Fig. 7 in LR2). The maximum near the surface forms as a result of the surface sensible and latent heat fluxes, while the maximum in the cloud forms due to a combination of latent heat release at cloud base and radiative cooling at cloud top. In a classic ScTBL, however, the cloud-top radiative cooling is so strong that it is able to mix the entire boundary layer.

(The surface fluxes are also weak in the classic ScTBL; thus, they do not provide any resistance to mixing from above.) The turbulence statistics in the classic ScTBL are more typical of free convection where there is only a single peak in $w'w'$ (see Fig. 5).

What we see in ASTEX is a double peak, with a very weak minimum in between. If we decrease that minimum a little, it becomes a TWBL profile, and if we increase it a little, it becomes a more classic ScTBL profile. This is a perfect example of the transitional nature of ASTEX. The Utrecht LES agrees with ADHOC in the cloud, and it also shows a hint of a secondary peak in the subcloud

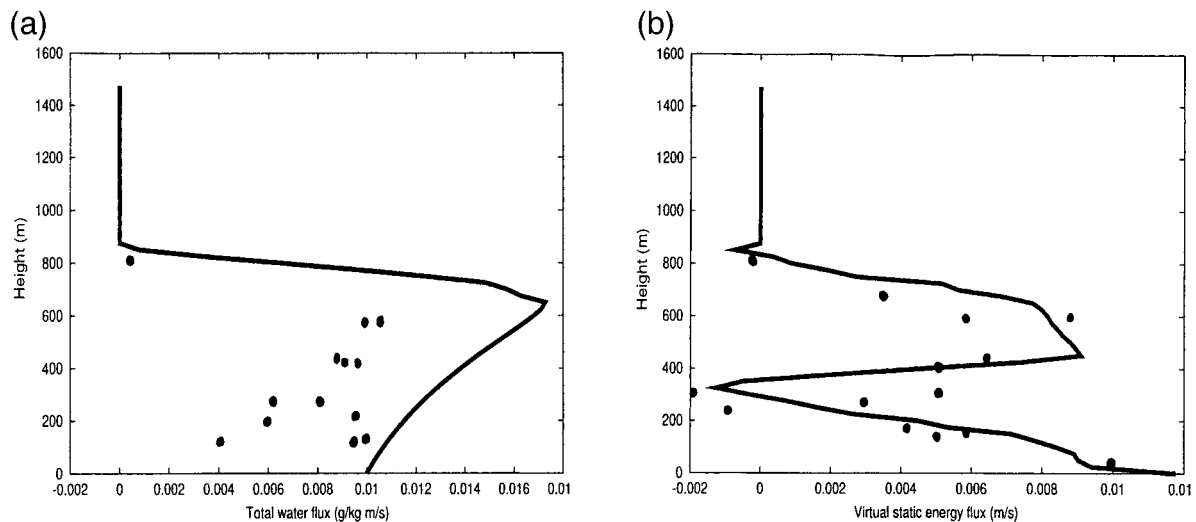


FIG. 14. Comparison of the ADHOC-simulated fluxes of (a) total water and (b) virtual static energy with those observed by aircraft for ASTEX. The darkest line is ADHOC and the dots are aircraft observations from the NCAR Electra as analyzed by de Rooze and Duijnkerke (1997).

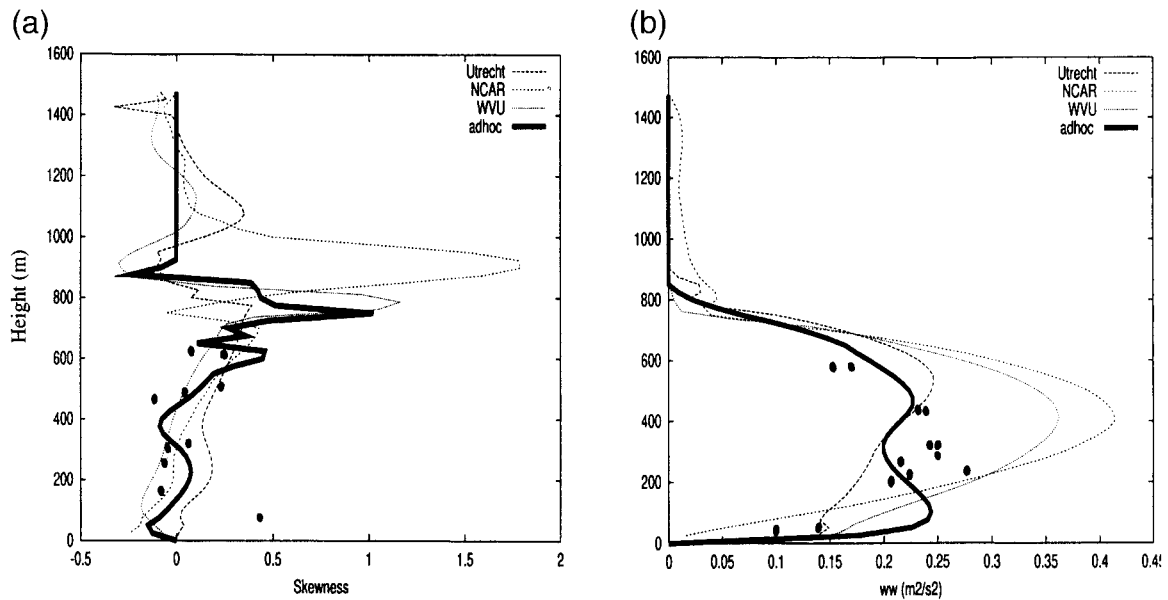


FIG. 15. Comparison of the (a) simulated skewness and (b) vertical velocity variance with those simulated by LES and observed. The darkest line is ADHOC, the lighter lines are the indicated LES models, and the dots are aircraft observations from the NCAR Electra as analyzed by de Roode and Duynkerke (1997).

layer. The other LES profiles do not show a double peak unless drizzle is included (see results from ASTEX GCSS case 209D available online at <http://www.fys.ruu.nl/~www.imau/ASTEX/astexcomp.html>). The magnitude of the observed $\overline{w'w'}$ profile agrees with that simulated by ADHOC, although due to scatter it is difficult to see a double peak.

Also shown in Fig. 15 is a comparison of the vertical velocity skewness with that observed from aircraft. The skewness profiles simulated by ADHOC agree nicely with the observed skewness, as well as the skewness simulated by LES. These profiles are physically realistic. Near the surface, the skewness is close to zero, indicating that the updraft area fraction is approximately 1/2. This is a result of weak surface fluxes. At cloud top, the skewness is negative, indicating the presence of narrow downdrafts. This is physically the result of cloud-top radiative cooling. Finally, near cloud base, condensational heating creates positive skewness.

Finally, we compare the ADHOC-simulated TKE budget profiles to those simulated by LES (Fig. 16). The largest difference occurs in the buoyancy profile. In the cloud layer, this difference is a direct result of the difference in the simulated radiative cooling between ADHOC and the LES models. ADHOC closely resembles the observations (Fig. 14), and as discussed above, some LES models that included drizzle have buoyancy profiles close to those observed. For the other simulated components of the TKE budget, the ADHOC and LES results agree quite nicely.

From this analysis, we can see that the LES models do not agree over the state of decoupling for this ASTEX case. Thus, this regime may not provide a critical test of

the ability of ADHOC to simulate the cloud regime that occurs between the TWBL and the classic ScTBL. However, as discussed above, several aspects of ADHOC's results point to weak decoupling between the cloud and subcloud layers, a feature that is realistic for clouds in the Sc-to-Cu transition regime. Modeling the time-dependent Sc-to-Cu transition is left for future work.

5. Summary and conclusions

In LR1, we used plume equations describing the mean properties of updrafts and downdrafts and used the framework of Randall et al. (1992) to derive a set of higher-order prognostic equations. This resulted in a combined MFC-HOC model whose equations are term-by-term consistent with the corresponding conventional HOC equations. The potential applicability of such an approach in large-scale models is wide ranging. As discussed, GCMs currently use separate schemes for PBL processes, shallow and deep Cu convection, and stratiform clouds. These schemes may individually work well in their respective regimes. However, these regimes are not always distinct (often, two or more may coexist). GCMs tend to poorly represent the total effect of clouds in these multiple-cloud regimes (Randall et al. 1998). Thus, there is a need to combine these parameterizations. The current ADHOC approach is a first step toward unifying cloud and boundary layer processes in large-scale models. In order to show the versatility of the ADHOC approach, we applied the model to a variety of atmospheric boundary layers including cloud-free convection, marine stratocumulus, and trade wind cumulus.

In general, ADHOC was successful at capturing many

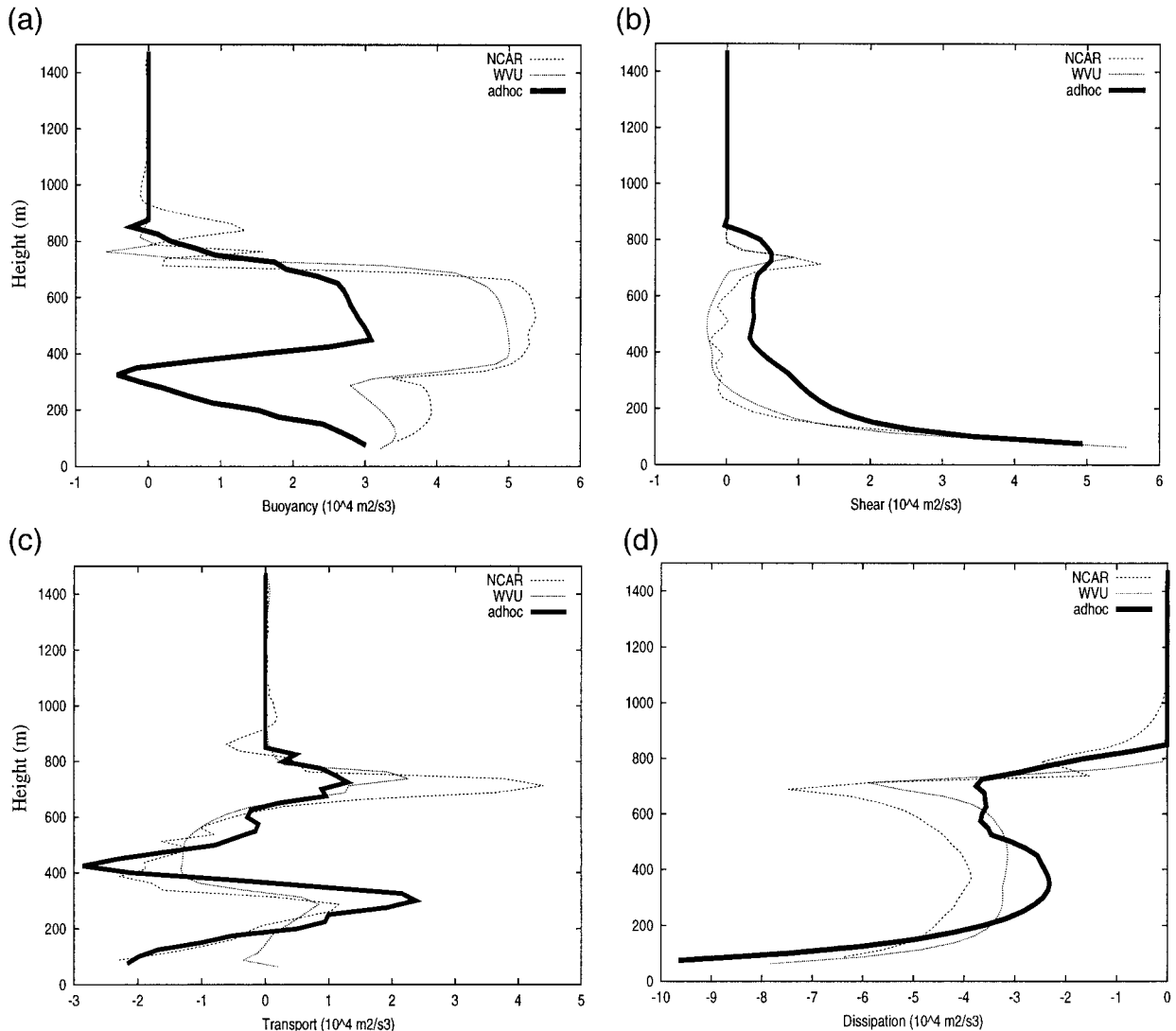


FIG. 16. Comparison of the simulated ADHOC TKE budgets with LES for ASTEX. (a) Buoyancy, (b) shear, (c) transport, (d) dissipation. The darkest line is ADHOC and the lighter lines are the indicated LES models.

of the physical features of these varied boundary layers. However, despite the success, a weakness of the current version of the model became apparent during these simulations: Entrainment is too weak in simulations where radiative cooling is not a prominent factor. Tests have shown that 1) the pressure parameterization in ADHOC is partly responsible for this problem (Lappen 1999) and 2) entrainment depends weakly on grid resolution for each of the regimes simulated.

Below, we briefly summarize the results of the three cases discussed in this paper.

a. Wangara

The Wangara data exemplify pure convection, driven by surface heating. The physics of this regime were adequately simulated by ADHOC. The simulated mean

state was fairly well mixed; the heat flux was linear from the surface up through the entrainment zone, where it became negative in response to entrainment of the warmer water from above; the vertical velocity variance was parabolic in shape with a maximum in the lower to middle boundary layer, as a result of the vertical acceleration experienced by thermals as they rise; and the temperature variance was a maximum near the surface and near the inversion.

b. BOMEX

BOMEX is a classic trade wind cumulus case, where the cloud fractions were observed to be near 20%. Accurately parameterizing this regime is critical in GCMs. The simulation of this regime is complicated by dry downdrafts and a positively skewed boundary layer.

Overall ADHOC was able to capture the three-layered structure associated with this regime. The mean state profiles agreed nicely with observations and the other LES models. However, the simulated liquid water mixing ratio in the cloud was too large. This was true despite a buoyancy flux that agreed with that simulated by LES. While weak entrainment may have played a role in the overprediction of liquid water, the apparent discrepancy between the simulated liquid water and buoyancy profiles was shown to be a result of the skewness being underpredicted (Fig. 11). The shape and magnitude of the simulated fluxes agree with both LES and observations. The TKE budget was in agreement with that simulated by LES. Thus, we see that ADHOC is able to reasonably represent the shape and magnitude of many of the typically observed profiles in the TWBL.

c. ASTEX

Marine stratocumulus clouds are globally important from both radiative and dynamical standpoints. Entrainment plays a major role in the evolution of this regime, but we found that the weak entrainment problem found in BOMEX and Wangara does not occur in this regime. While we would expect enhanced entrainment due to evaporative cooling, this did not explain why ADHOC overpredicted the entrainment rate relative to LES. One possible explanation is that a large fraction of the radiative cooling occurred within the inversion. This was shown by Lewellen and Lewellen (1998) to be responsible for enhanced entrainment in models that do not accurately resolve the inversion. Many of the simulated fields in ASTEX distinctly reflect the transitional nature of the case (e.g., $w'w'$ and $w's'_v$). This is extremely encouraging from the GCM perspective because these transitional regimes are exactly the ones for which GCMs currently perform poorly. The only major difference between the ADHOC simulation and the aircraft observations was that the total water flux in ADHOC was larger than observed (Fig. 14). This was attributed to the large simulated entrainment drying at cloud top and to the exclusion of drizzle in the simulation.

In conclusion, ADHOC appears to have the potential to represent both cloud and boundary layer processes. However, the current version of ADHOC is not GCM-ready for several reasons. First of all, a grid resolution of 50 m (or less) and a time step of 0.5 s are not feasible for use in GCMs. We must be able to represent turbulence in the PBL using much coarser resolution. In the middle of the PBL, coarser resolution is often all that is needed because the fields are smoothly varying in the vertical. However, near the surface and near the inversion, physically important turbulence-generating or -dissipating mechanisms are concentrated on finer scales. In the few tens of meters near the surface, surface layer similarity can be used to diagnose the turbulence statistics, and thus fine resolution is not required in this region. However, the PBL-top inversion must be ade-

quately resolved to accurately represent the effects of clouds. One way to avoid the need for high resolution near the inversion is to use a modified “sigma” coordinate (Suarez et al. 1983). This is a stretched vertical coordinate in which the PBL top is a layer edge.

We believe that ADHOC has the potential to provide a unified framework for cumulus and boundary layer processes. In the future, we hope to generalize the probability density function in ADHOC and derive a more realistic, more flexible model. We are also working to develop an ADHOC-consistent pressure parameterization so that we can capture the important contribution of these terms to the structure and evolution of the turbulent regime, which we are trying to represent. Our long-term goal is a unified parameterization that will combine the PBL and cumulus parameterizations in a single physical and computational framework.

Acknowledgments. This research was funded by the National Aeronautics and Space Administration under Grant NAG1-1701 and Contract 960700 through the Jet Propulsion Laboratory, and by the National Science Foundation under Grant OPP9504246, all to Colorado State University. Computing support was obtained from the Scientific Computing Division of the National Center for Atmospheric Research.

REFERENCES

- Albrecht, B. A., 1979: A model of the thermodynamic structure of the trade-wind boundary-layer. Part II. Applications. *J. Atmos. Sci.*, **36**, 90–98.
- , D. Johnson, W. H. Schubert, and A. S. Frisch, 1995: The Atlantic stratocumulus transition experiment—ASTEX. *Bull. Amer. Meteor. Soc.*, **76**, 889–904.
- André, J. C., G. De Moor, P. Lacarrere, G. Therry, and R. Du Vachat, 1978: Modeling the 24-hour evolution of the mean and turbulent structures of the planetary boundary layer. *J. Atmos. Sci.*, **35**, 1861–1883.
- Arakawa, A., and W. H. Schubert, 1974: The interaction of a cumulus cloud ensemble with the large-scale environment, Part I. *J. Atmos. Sci.*, **31**, 674–701.
- Bechtold, P., 1992: A model of marine boundary-layer cloudiness for mesoscale applications. *J. Atmos. Sci.*, **49**, 1723–1744.
- , J. W. M. Cuijpers, P. Mascart, and P. Trouilhet, 1995: Modeling of trade wind cumuli with a low-order turbulence model: Toward a unified description of Cu and Sc clouds in meteorological models. *J. Atmos. Sci.*, **52**, 455–463.
- , S. K. Krueger, W. S. Lewellen, E. van Meijgaard, C.-H. Moeng, D. A. Randall, A. van Ulden, and S. Wang, 1996: Modeling a stratocumulus-topped PBL: Intercomparison among different one-dimensional codes and with large eddy simulation. *Bull. Amer. Meteor. Soc.*, **77**, 2033–2042.
- Betts, A., 1973: Non-precipitating cumulus convection and its parameterization. *Quart. J. Roy. Meteor. Soc.*, **99**, 178–196.
- , 1976: Modeling subcloud layer structure and interaction with a shallow cumulus layer. *J. Atmos. Sci.*, **33**, 2363–2382.
- , 1990: Diurnal variation of California coastal stratocumulus from two days of boundary layer soundings. *Tellus*, **42A**, 302–304.
- Bougeault, P., 1981a: Modeling the trade wind cumulus boundary layer. Part II: High-order one-dimensional model. *J. Atmos. Sci.*, **38**, 2414–2428.
- , 1981b: Modeling the trade wind cumulus boundary layer. Part

- II: High-order one-dimensional model. *J. Atmos. Sci.*, **38**, 2429–2439.
- , 1982: Cloud-ensemble relations based on the gamma probability distribution for the higher order models of the planetary boundary layer. *J. Atmos. Sci.*, **39**, 2691–2700.
- , and J. C. André, 1986: On the stability of the third-order turbulence closure for the modeling of the stratocumulus-topped boundary layer. *J. Atmos. Sci.*, **43**, 1574–1581.
- Bretherton, C. S., and R. Pincus, 1995: Cloudiness and marine boundary layer dynamics in the ASTEX Lagrangian experiments. Part I: Synoptic setting and vertical structure. *J. Atmos. Sci.*, **52**, 2707–2723.
- Brost, R. A., J. C. Wyngaard, and D. H. Lenschow, 1982: Marine stratocumulus layers. Part II: Turbulence budgets. *J. Atmos. Sci.*, **39**, 818–836.
- Browning, K. A., 1994: Survey of perceived priority issues in the parameterizations of cloud-related processes. *Quart. J. Roy. Meteor. Soc.*, **120**, 483–487.
- Chen, C., and W. R. Cotton, 1983: One-dimensional simulation of the stratocumulus-capped mixed layer. *Bound.-Layer Meteor.*, **25**, 289–321.
- Clark, R. H., A. J. Dyer, R. R. Brook, D. G. Reid, and A. J. Troup, 1971: The Wangara experiment: Boundary layer data. Tech. paper 19, Division Meteor. Phys. CSIRO, Australia.
- Cuijpers, J. W. M., and P. G. Duynkerke, 1993: Large eddy simulation of trade wind cumulus clouds. *J. Atmos. Sci.*, **50**, 3894–3908.
- Deardorff, J. W., 1980: Cloud top entrainment instability. *J. Atmos. Sci.*, **37**, 131–147.
- de Laat, A. T. J., and P. G. Duynkerke, 1998: Analysis of ASTEX-stratocumulus observational data using mass-flux approach. *Bound.-Layer Meteor.*, **86**, 63–87.
- de Roode, S. R., and P. G. Duynkerke, 1997: Observed Lagrangian transition of stratocumulus into cumulus during ASTEX: Mean state and turbulence structure. *J. Atmos. Sci.*, **54**, 2157–2173.
- Duynkerke, P. G., H. Q. Zhang, and P. J. Jonker, 1995: Microphysical and turbulent structure of nocturnal stratocumulus as observed during ASTEX. *J. Atmos. Sci.*, **52**, 2763–2777.
- Esbensen, S., 1978: Bulk thermodynamic effects and properties of small tropical cumuli. *J. Atmos. Sci.*, **35**, 826–837.
- Gregory, D., and P. R. Rowntree, 1990: A mass flux convection scheme with representation of cloud ensemble characteristics and stability-dependent closure. *Mon. Wea. Rev.*, **118**, 1483–1506.
- Hanson, H. P., 1981: On mixing by tradewind cumuli. *J. Atmos. Sci.*, **38**, 1003–1014.
- Harrison, E. F., F. P. Minnis, B. R. Barkstrom, V. Ramanathan, R. D. Cess, and G. G. Gibson, 1990: Seasonal variation of cloud radiative forcing derived from the Earth Radiation Budget Experiment. *J. Geophys. Res.*, **95**, 18 687–18 703.
- Hartmann, D. L., M. E. Ockert-Bell, and M. L. Michelsen, 1992: The effect of cloud type on Earth's energy balance. *J. Climate*, **5**, 1281–1304.
- Hicks, B. B., 1978: An analysis of Wangara micrometeorology: Surface stresses, sensible heat, evaporation, and dewfall. NOAA Tech. Memo. ERL ARL-104, Air Resources Laboratory, Silver Spring, MD, 36 pp.
- Holtzlag, A. A. M., and C.-H. Moeng, 1991: Eddy diffusivity and countergradient transport in the convective atmospheric boundary layer. *J. Atmos. Sci.*, **48**, 1690–1698.
- Krueger, S. K., 1988: Numerical simulation of tropical cumulus clouds and their interaction with the subcloud layer. *J. Atmos. Sci.*, **45**, 2221–2250.
- , and A. Bergeron, 1994: Modeling the trade cumulus boundary layer. *Atmos. Res.*, **33**, 169–192.
- Lappen, C.-L., 1999: The unification of mass flux and higher-order closure in the simulation of boundary layer turbulence. Ph.D. thesis, Colorado State University, 330 pp.
- , and D. A. Randall, 2001a: Toward a unified parameterization of the boundary layer and moist convection. Part I: A new type of mass-flux model. *J. Atmos. Sci.*, **58**, 2021–2036.
- , and —, 2001b: Toward a unified parameterization of the boundary layer and moist convection. Part II: Lateral mass exchanges and subplume-scale fluxes. *J. Atmos. Sci.*, **58**, 2037–2051.
- Launder, 1975: On the effects of a gravitational field on the turbulent transport of heat and momentum. *J. Fluid Mech.*, **67**, 569–581.
- Lewellen, D. C., and W. S. Lewellen, 1998: Large-eddy boundary layer entrainment. *J. Atmos. Sci.*, **55**, 2645–2665.
- Lilly, D. K., 1968: Models of cloud-topped mixed layers under a strong inversion. *Quart. J. Roy. Meteor. Soc.*, **94**, 292–309.
- Lumley, J. L., 1978: Computational modeling of turbulent flows. *Advances in Applied Mechanics*. Vol. 18. Academic Press, 123–176.
- Mellor, G. L., and T. Yamada, 1974: A hierarchy of turbulence closure models for planetary boundary layers. *J. Atmos. Sci.*, **31**, 1791–1806.
- Moeng, C.-H., 1984: A large-eddy simulation for the study of planetary boundary layer turbulence. *J. Atmos. Sci.*, **41**, 2052–2062.
- , and A. Arakawa, 1980: Numerical study of a marine subtropical stratus cloud layer and its stability. *J. Atmos. Sci.*, **37**, 2661–2676.
- , and D. A. Randall, 1984: Problems in simulating the stratocumulus-topped boundary layer with a third-order closure model. *J. Atmos. Sci.*, **41**, 1588–1600.
- Nicholls, S., 1984: Dynamics of stratocumulus: Aircraft observations and comparisons with a mixed layer model. *Quart. J. Roy. Meteor. Soc.*, **110**, 783–820.
- , 1989: The structure of radiatively-driven convection in stratocumulus. *Quart. J. Roy. Meteor. Soc.*, **115**, 487–511.
- Nitta, T., 1975: Observational determination of cloud mass flux distributions. *J. Atmos. Sci.*, **32**, 73–91.
- Oliver, D. A., W. S. Lewellen, and G. G. Williamson, 1978: Interaction between turbulent and radiative transport in the development of fog and low-level stratus. *J. Atmos. Sci.*, **35**, 301–316.
- Penc, R. S., and B. Albrecht, 1987: Parametric representation of heat and moisture fluxes in cloud-topped mixed layers. *Bound.-Layer Meteor.*, **38**, 225–248.
- Pennel, W. T., and M. A. Lemone, 1974: Experimental study of turbulence structure in the fair-weather trade wind boundary layer. *J. Atmos. Sci.*, **31**, 1308–1323.
- Ramanathan, V., 1989: Cloud-radiative forcing and climate: Results from the Earth Radiation Budget Experiment. *Science*, **243**, 57–63.
- Randall, D. A., 1980: Conditional instability of the first kind upside-down. *J. Atmos. Sci.*, **37**, 125–130.
- , and M. J. Suarez, 1984: On the dynamics of stratocumulus formation and dissipation. *J. Atmos. Sci.*, **41**, 3052–3057.
- , Q. Shao, and C.-H. Moeng, 1992: A second-order bulk boundary-layer model. *J. Atmos. Sci.*, **49**, 1903–1923.
- , —, and M. Branson, 1998: Representation of clear and cloudy boundary layers in climate models. *Clear and Cloud Boundary Layers*, A. A. M. Holtslag and P. G. Duynkerke, Eds., Royal Netherlands Academy of Arts and Sciences, 305–322.
- Rotta, J. C., 1951: Statistische Theorie Nichtthomogener Turbulenz 2. *Z. Phys.*, **131**, 51–77.
- Siebesma, A. P., and J. W. M. Cuijpers, 1995: Evaluation of parametric assumptions for shallow cumulus convection. *J. Atmos. Sci.*, **52**, 650–666.
- Siems, S. T., C. S. Bretherton, M. B. Baker, S. Shy, and R. E. Breidenthal, 1990: Buoyancy reversal and cloud-top entrainment instability. *Quart. J. Roy. Meteor. Soc.*, **116**, 705–739.
- Slingo, A., 1990: Sensitivity of the Earth's radiation budget to changes in low clouds. *Nature*, **343**, 49–51.
- Somméria, G., 1976: Three-dimensional simulation of turbulent processes in an undisturbed trade wind boundary layer. *J. Atmos. Sci.*, **33**, 216–241.
- , and J. W. Deardorff, 1977: Subgrid-scale condensation in models of nonprecipitating clouds. *J. Atmos. Sci.*, **34**, 344–355.
- Stull, R. B., 1988: *An Introduction to Boundary Layer Meteorology*. Kluwer Academic, 666 pp.
- Suarez, M. J., A. Arakawa, and D. A. Randall, 1983: The param-

- terization of the planetary boundary layer in the UCLA general circulation model: Formulation and results. *Mon. Wea. Rev.*, **111**, 2225–2243.
- Sun, W.-Y., and Y. Ogura, 1980: Modeling the evolution of the convective planetary boundary layer. *J. Atmos. Sci.*, **37**, 1558–1572.
- Tiedtke, M., 1988: Parameterization of cumulus convection in large-scale models. *Physically-Based Modeling and Simulation of Climate and Climate Change*, M. Schlesinger, Ed., D. Reidel, 375–431.
- , 1989: A comprehensive mass flux scheme for cumulus parameterization in large-scale models. *Mon. Wea. Rev.*, **117**, 1779–1800.
- Turton, J. D., and S. Nicholls, 1987: Study of the diurnal variation of stratocumulus using a multiple mixed-layer model. *Quart. J. Roy. Meteor. Soc.*, **113**, 969–1009.
- Wang, S., and B. Albrecht, 1986: Stratocumulus model with an internal circulation. *J. Atmos. Sci.*, **43**, 2374–2391.
- , and ———, 1990: A mean gradient of the convective boundary layer. *J. Atmos. Sci.*, **47**, 126–138.
- , and Q. Wang, 1994: Roles of drizzle in a one-dimensional third-order turbulence closure model of the nocturnal stratified marine boundary layer. *J. Atmos. Sci.*, **51**, 1559–1576.
- , and B. Stevens, 2000: Top-hat representation of turbulence statistics in cloud-topped boundary layers: A large eddy simulation study. *J. Atmos. Sci.*, **57**, 423–441.
- Willis, G. E., and J. W. Deardorff, 1974: Laboratory model of the unstable planetary boundary layer. *J. Atmos. Sci.*, **31**, 1297–1307.
- Wyngaard, J. C., and O. R. Coté, 1974: The evolution of a convective planetary boundary layer. *Bound-Layer Meteor.*, **7**, 289–308.
- Yamada, T., and G. L. Mellor, 1975: Simulation of the Wangara atmospheric boundary layer data. *J. Atmos. Sci.*, **32**, 2309–2329.
- , and ———, 1979: A numerical simulation of BOMEX data using a turbulence closure model coupled with ensemble cloud relations. *Quart. J. Roy. Meteor. Soc.*, **105**, 915–944.
- Yanai, M., J. H. Chu, T. E. Stark, and T. Nitta, 1976: Response of deep and shallow tropical marine cumuli to large-scale processes. *J. Atmos. Sci.*, **33**, 976–991.
- Young, G. S., 1988: Turbulence structure of the convective boundary layer. Part II: Phoenix 78 aircraft observations of thermals and their environment. *J. Atmos. Sci.*, **45**, 727–735.